Locating tectonic tremors with uncertainty estimates: Time- and amplitude-difference optimization, wave propagation-based quality control, and Bayesian inversion

Takeshi Akuhara[1], Yusuke Yamashita[2], Hiroko Sugioka[3], Masanao Shinohara[1]

[1]Earthquake Research Institute, The University of Tokyo
[2]Disaster Prevision Research Institute, Kyoto University
[3] Department of Planetology, Graduate School of Science, Kobe University

Summary

The accurate location of tectonic tremors helps improve understanding of their underlying physical processes. However, current location methods often do not statistically evaluate uncertainties to a satisfactory degree and do not account for potential biases due to subsurface structures not included in the model. To address these issues, we propose a novel three-step process for locating tectonic tremors. First, the measured time- and amplitude differences between station pairs are optimized to obtain station-specific relative time and amplitude measurements with uncertainty estimates. Second, the time– and amplitude–distance relationships in the optimized data are used to roughly estimate the propagation speed (i.e., shear wave velocity) and attenuation strength. Linear regression is applied to each event, and the resulting velocity and attenuation strength are used for quality control. Finally, the tremor location problem is formulated within a Bayesian framework where the model parameters include the source locations, local site delay/amplification factors, shear wave velocity, and attenuation strength. The Markov chain Monte Carlo algorithm is used to sample the posterior probability and is augmented by a parallel tempering scheme for an efficient global search. We tested the proposed method on ocean-bottom data indicating an intense episode of tectonic tremors in Kumano-nada within the Nankai Trough subduction zone. The results show that the range of the 95% confidence interval is typically <7 km horizontally and <10 km vertically. A series of experiments with different inversion settings reveals that adopting amplitude data and site correction factors help reduce random error and systematic bias, respectively. Probabilistic sampling allows us to spatially map the probability of a tremor occurring at a given location. The probability map is used to identify lineaments of tremor sources, which provides insights into structural factors that favor tremor activity.

Key words

Computational seismology, Body waves, Inverse theory, Subduction zone processes,

Seismicity and tectonics

1. Introduction

Tectonic tremors, considered as a swarm of low-frequency earthquakes, constitute a broad spectrum of slow earthquakes together with very low-frequency earthquakes and slow-slip events. They were first discovered in southwestern Japan (Obara, 2002) and have since been identified at subducting plate interfaces worldwide (Araki et al., 2017; Brown et al., 2005; Nishikawa et al., 2019; Payero et al., 2008; Plata-Martinez et al., 2021; Rogers, 2003; Todd et al., 2018; Yamashita et al., 2015). Slow earthquakes, including tectonic tremors, release seismic energy over a long time considering their magnitudes, which indicates that they may be governed by different physical processes than regular earthquakes (Ide et al., 2007). Owing to their proximity to the rupture areas of megathrust earthquakes, slow earthquakes have drawn significant attention for their potential to deepen our understanding of future devastating earthquakes (Obara & Kato, 2016).

The accurate location of tectonic tremors is vital to understanding the slip behavior of plate interfaces. The spatiotemporal evolution of tectonic tremors has several unique but ubiquitous characteristics. First, tremors occur episodically, with their epicenters migrating parallel to the subduction margin, which indicates the simultaneous occurrence of slow-slip events. Second, tremors occasionally back-propagate against their main front at distinctly high speeds, known as rapid tremor reversal (e.g., Houston et al., 2011). Third, streaks of tremors in the dip direction of the subducting plate have been observed (e.g., Ghosh et al., 2010). These spatiotemporal patterns of tremors can constrain the frictional properties of the plate interface (Rubin, 2011), underlying physical processes (Cruz-Atienza et al., 2018), and structural factors that cause tremors (Ide, 2010).

The signals of tectonic tremors emerge without a clear phase onset, which makes locating them using the same methods as for regular earthquakes impractical. A common approach is the envelope correlation method (e.g., Mizuno & Ide, 2019; Obara, 2002), which cross-correlates enveloped seismograms between pairs of stations and assumes that the resulting time lag represents a difference in S-wave travel time. Optimization methods can then be applied to determine the source locations that best explain the measured arrival time differences. Another approach is to use the amplitude (e.g., Husker et al., 2012; Ogiso & Tamaribuchi, 2022), although such techniques are more widely used for locating volcanic tremors rather than tectonic tremors. Because seismic waves lose energy during propagation, the spatial pattern of amplitudes can provide clues about source locations. However, this approach requires knowledge of attenuation structures and local site amplification, which typically necessitates additional analysis. Some studies have used a joint approach that combines both time- and amplitude-based methods, where the different datasets are often weighted subjectively (Maeda & Obara, 2009).

Despite the importance of investigating the source locations of tectonic tremors, many studies have not formally estimated the uncertainties associated with these locations, with only a few exceptions (e.g., Bombardier et al., 2023; McCausland et al., 2010). The lack of uncertainty estimation increases the risk of misinterpreting results. Accurately estimating the uncertainties of tremor locations requires considering the statistics of the input measurements in the data domain (i.e., time and amplitude domains) and then converting them into the spatial domain by forward calculation. Uncertainties in the structure model used for the forward calculation must also be considered to prevent systematic biases. Such uncertainties in structures would be severe for offshore studies targeting shallow tectonic tremors (e.g., Yamashita et al., 2015). Typically, the seafloor is covered with unconsolidated sediments. Such near-surface structures amplify the amplitude and delay the arrival of seismic waves, and the degree of this effect varies according to the geographic location.

To address the above issues, we propose a three-step method for locating tectonic tremors and estimating their uncertainty, which we applied to real tremor data obtained at Kumano-nada in the Nankai Trough subduction zone as a demonstration.

2. Data

We collected data from a seismic network at Kumano-nada in the Nankai Trough subduction zone, where the Philippine Sea plate subducts beneath the fore-arc margin. As shown in Fig. 1, the network comprises 16 permanent cabled stations from the Dense Ocean Network for Earthquake and Tsunamis (DONET) (Kaneda et al., 2015; Kawaguchi et al., 2015) and 15 ocean-bottom seismometers (OBSs) temporarily installed from September 2019 to June 2021. All OBSs were equipped with three-component short-period velocity sensors with a natural frequency of 1 Hz. The network includes two micro subarrays (SHM6 and SHM7) each comprising five OBSs.

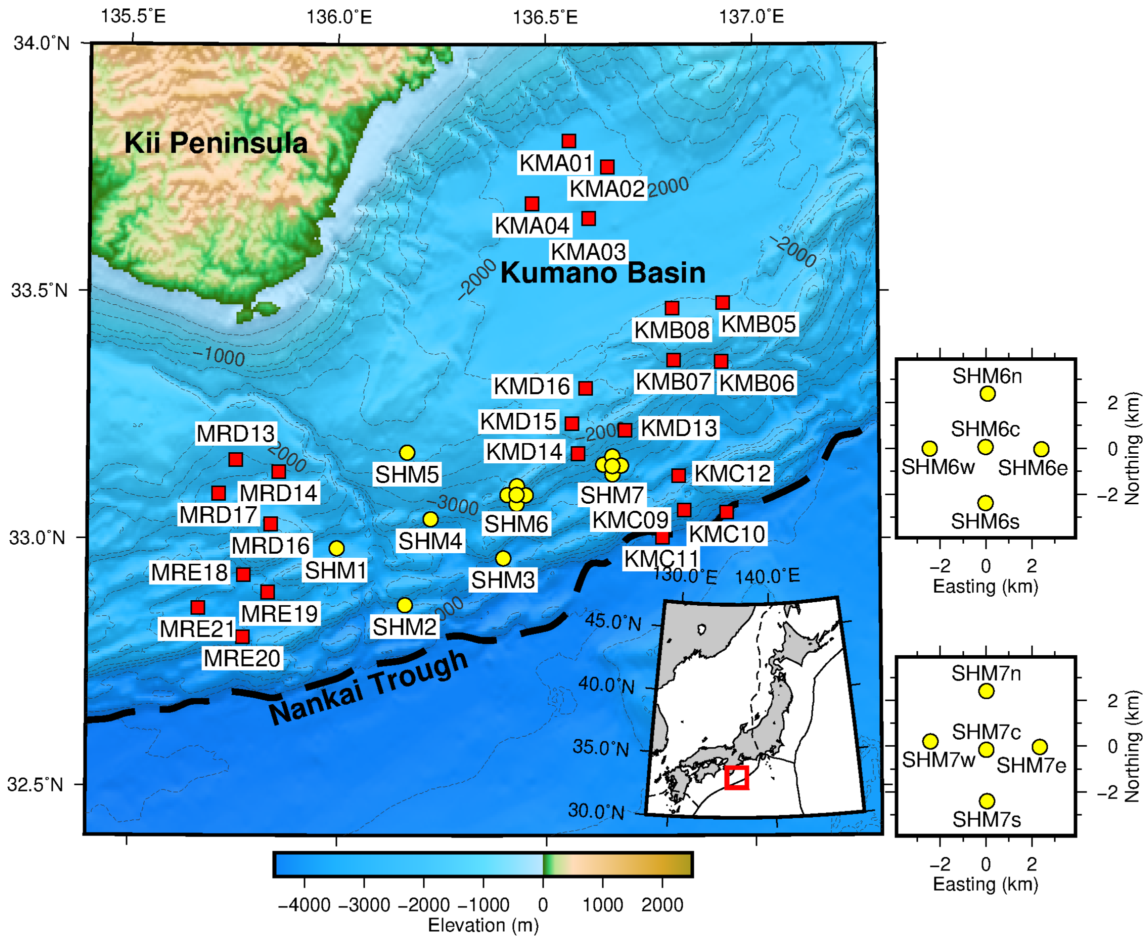

Figure 1. Tectonic setting and station arrangement of the study area. The red squares are permanent DONET stations, and the yellow circles are temporary ocean-bottom seismometers (OBSs), which include two micro subarrays (SHM6 and SHM7) each comprising five OBSs with a separation distance of ~2.5 km (right panels). The inset shows the configuration of tectonic plates around Japan, where the red square encloses the study area.

Intense episodes of slow earthquakes, including tectonic tremors and very low-frequency earthquakes, repeatedly occur in this region at intervals of ~5 years (e.g., Takemura et al., 2022). The latest episode began on December 6, 2020, and persisted for approximately 2 months (Ogiso & Tamaribuchi, 2022) within the observation period of the OBSs. We collected data from a 85-day period including this episode, from December 6, 2020 to February 28, 2021.

To detect tectonic tremors, we preprocessed continuous seismic waveform data as follows. First, 300-s time segments were successively extracted from the continuous data with 50% overlap. The extracted time series were corrected for instrument response, detrended, tapered, 1–10 Hz bandpass-filtered, and converted to envelopes via the Hilbert transform. We then smoothed the resulting envelopes with a 6-s triangular filter and merged the two horizontal components by using the root sum squared method. We did not use the vertical component because shear waves dominate the seismic records of tectonic tremors. Finally, the data were decimated from 100 to 1 sample per second.

Every 150 s, we evaluated the existence of tremor signals in the subsequent 300-s time segment by calculating inter-station cross-correlation. This involved cross-correlating the 300-s envelopes over a lag time from -150 to 150 s for each station pairs, and we deemed a tremor detected if the maximum value in the cross-correlation function exceeded a threshold for at least 300 station pairs. The threshold was set uniquely for each station pair, based on the 98th percentile of the histogram of correlation values (Fig. 2a). Fig. 2(b) summarizes the resulting thresholds from all station pairs. In general, smaller station separation distances corresponds to higher thresholds, with values spanning from 0.38 to 0.84. This detection analysis was conducted on approximately 50,000 sets of envelopes, leading to the identification of 34,068 tremor events.

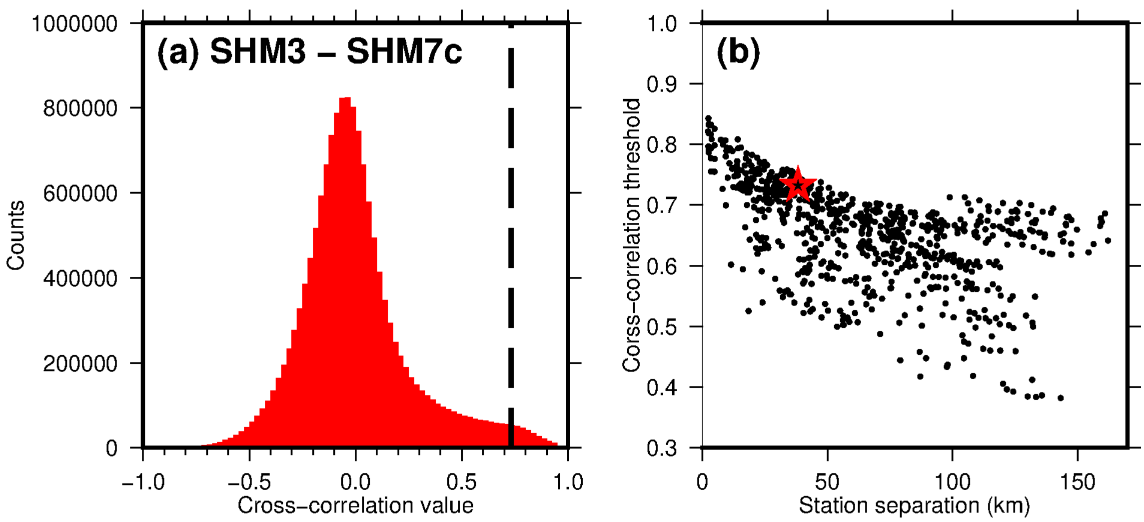

Figure 2. (a) Histogram of cross-correlation values for the station pair SHM3 and SHM7c. The dashed line indicates the 98% percentile, which is used as the detection threshold. Note that the envelopes were subtracted by their mean amplitude before calculating the cross-correlation function, and thus the correlation value can be negative. (b) Detection threshold by cross-correlation value against the separation distance between stations. The red star corresponds to the station pair SHM3 and SHM7c, which is shown in (a).

We recognize inherent limitations of the above detection process. First, the detection process cannot distinguish the origin of high correlation values, which could stem from various sources, such as distant earthquakes, artificial sources from seismic survey, or even random environmental noise. The high number of detections likely indicates a number of false detections of such non-tremor signals. Second, the detection process assumes a maximum of one tremor occurring within a 300-s time segment. Multiple tremors in a single time segment may lead to an unreliable source location in the later inversion analysis. However, we emphasize that the quality control process proposed later in Section 3.2 has the potential to alleviate these two issues by quantitatively evaluating wave propagation patterns. The other issue is that a single event may be detected twice due to the 50% overlap of adjacent time segments. This redundancy can be resolved after determining the source location.

3. Method

Our proposed method has three steps. Step 1 is to optimize measurements from station pairs such as the arrival time difference and logarithmic amplitude ratio, which outputs the relative arrival time and logarithmic amplitude ratio at each station along with their respective uncertainties. These uncertainties are obtained from the redundancy in the station pair measurements and can be incorporated in the final inversion stage to acquire uncertainties in the spatial domain. Step 2 is to extract the first-order features of wave propagation from the optimized station-specific data: the propagation speed and attenuation strength. These features are then used as quality control factors to retain good-quality data. Step 3 is to invert the station-specific data and their uncertainties for hypocenters by using the Markov chain Monte Carlo (MCMC) algorithm in a Bayesian framework. To address biases from unknown structures, we jointly solve multiple hypocenters and include structural parameters and the associated correction factors in the model parameters.

3.1. Step 1: Optimization of arrival time and amplitude differences

The unclear phase onset makes direct measurements of the arrival times of tectonic tremors a challenge. A widely used alternative approach is to use cross-correlation to measure the arrival time difference between station pairs (e.g., Obara, 2002):

$$\Delta t_{ij} = \arg\max_{t'} \sum_{t} u_i(t+t')u_j(t), \tag{1}$$

where $u_i(t)$ is an envelope waveform recorded at the ith station and Δt_{ij} is the arrival time difference between the ith and jth stations. This approach only works when the two waveforms are sufficiently similar. If the waveforms differ (e.g., due to different propagation paths), the measured arrival time difference can deviate from the true value.

In addition, a high level of noise can easily pose artificial peaks in the cross-correlation functions. Once the arrival time difference is obtained, the amplitude ratio between the two envelopes is defined as follows:

$$\Delta a'_{ij} = \frac{\sum_t u_i(t + \Delta t_{ij}) u_j(t)}{\sum_t u_j(t) u_j(t)}. \tag{2}$$

This definition corresponds to the maximum likelihood estimation (MLE) of the amplitude ratio between two similar waveforms (Appendix A). The numerator has already been calculated to find the maximum of the cross-correlation function in Equation (1), so it does not require additional computation. Other definitions than Equation (2) may be used for the amplitude ratio, such as the squared sum (Maeda & Obara, 2009) or median value (Li et al., 2022). The obtained amplitude ratios are converted to amplitude differences by taking the logarithm so that they can be treated mathematically in the same manner as the arrival time differences:

$$\Delta a_{ij} \equiv \ln(\Delta a'_{ij}) = \ln \frac{\sum_t u_i(t + \Delta t_{ij}) u_j(t)}{\sum_t u_j(t) u_j(t)}. \tag{3}$$

The above process yields $N_{sta}(N_{sta} - 1)/2$ pairs of measurements, where N_{sta} is the number of stations. Individual pair measurements are dependent on other pairs (i.e., $\Delta t_{ij} \sim \Delta t_{ik} - \Delta t_{kj}$). In other words, the $N_{sta}(N_{sta} - 1)/2$ measurements inherently include redundancy. We may optimize this redundancy by solving a linear system (VanDecar and Crosson, 1990):

$$\begin{pmatrix} 1 & -1 & 0 & 0 & \cdots & 0 & 0 & 0 & 0 \\ 1 & 0 & -1 & 0 & \cdots & 0 & 0 & 0 & 0 \\ & & & & \vdots & & & & \\ 0 & 0 & 0 & 0 & \cdots & 0 & 1 & 0 & -1 \\ 0 & 0 & 0 & 0 & \cdots & 0 & 0 & 1 & -1 \\ 1 & 1 & 1 & 1 & \cdots & 1 & 1 & 1 & 1 \end{pmatrix} \begin{pmatrix} t_1^{rel} \\ t_2^{rel} \\ \vdots \\ t_{N_{sta}-1}^{rel} \\ t_{N_{sta}}^{rel} \end{pmatrix} = \begin{pmatrix} \Delta t_{12} \\ \Delta t_{13} \\ \vdots \\ \Delta t_{N_{sta}-2\, N_{sta}} \\ \Delta t_{N_{sta}-1\, N_{sta}} \\ 0 \end{pmatrix}, \tag{4}$$

where $t_1^{rel} \cdots t_{N_{sta}}^{rel}$ denote the relative arrival time of a tremor signal at each station. A regularization condition is added to the bottom row that imposes a zero-sum requirement on the relative arrival times (i.e., $\sum_{i=1}^{N_{sta}} t_i^{rel} = 0$). This regularization condition enables us to solve the system of Equation (4) in terms of t_i^{rel} in the least-square manner, but the resulting arrival times are only relative to other stations. Noting that $\Delta t_{ii} = 0$ from Equation (1), the least-square solution is given as follows (VanDecar & Crosson, 1990):

$$t_i^{rel} = \frac{1}{N_{sta}} \sum_{j=1}^{N_{sta}} \Delta t_{ij}. \tag{5}$$

This optimization reduces the redundant measurements of $N_{sta}(N_{sta} - 1)/2$ arrival time differences between station pairs to N_{sta} station-specific relative arrival times. The original redundancy provides insights into the uncertainty in the relative arrival times; in essence, relative arrival times would have larger uncertainties if the original arrival time differences (i.e., Δt_{ij}) are inconsistent among station pairs. For example, the standard deviation of the error on t_i^{rel} can be calculated as the sum of squared residuals associated with the ith station (VanDecar & Crosson, 1990):

$$\sigma_i^{time} = \sqrt{\frac{\sum_{j=1}^{N_{sta}} \left[\Delta t_{ij} - \left(t_i^{rel} - t_j^{rel}\right)\right]^2}{N_{sta} - 2}}. \tag{6}$$

It is important to note that Equation (6) provides conservative estimates of uncertainty, where relative arrival time is assumed uncertain only for the ith station. In other words, measurement error in Δt_{ij} is attributed solely to the ith station. Alternatively, if we assume that all stations have the same degree of uncertainty, the magnitude of σ_i^{time} decreases by $1/\sqrt{2}$ compared to the estimate provided by Equation (6). In this study, we adopt the conservative definition given by Equation (6) to minimize the risk of overinterpretation.

Similar equations hold for logarithmic amplitudes:

$$a_i^{rel} = \frac{1}{N_{sta}} \sum_{j=1}^{N_{sta}} \Delta a_{ij}\,, \tag{7}$$

and

$$\sigma_i^{amp} = \sqrt{\frac{\sum_{j=1}^{N_{sta}} \left[\Delta a_{ij} - \left(a_i^{rel} - a_j^{rel}\right)\right]^2}{N_{sta} - 2}}, \tag{8}$$

where a_i^{rel} is a relative logarithmic amplitude at the ith station, and σ_i^{amp} is the corresponding standard deviation.

In the later Bayesian inversion in Section 3.3, the relative arrival time (t_i^{rel}) and amplitude (a_i^{rel}) are used as input data, and the standard deviations (σ_i^{time} and σ_i^{amp}) are used for calculating the likelihood.

Fig. 3 demonstrates the effectiveness of the proposed method when applied to an example event. The envelopes exhibit improved waveform alignment after being shifted in time by the optimized values (Fig. 3a) and comparable amplitude levels after being scaled in amplitude (Fig. 3b). We found that the proposed optimization works well with good-quality data that shows high signal-to-noise ratios across the entire network. Typical failures involve an insufficient signal level at some stations, which results in poor temporal alignments by cross-correlation (Fig. S1). Such poor-quality data, even if present at only a few stations, can distort the optimized solution significantly because the optimized solutions given by the arithmetic mean (i.e., Equations (5) and (7)) are not robust against outliers. This sensitivity to poor-quality data requires an automatic and objective process to reject ill-optimized results, as proposed in the next section.

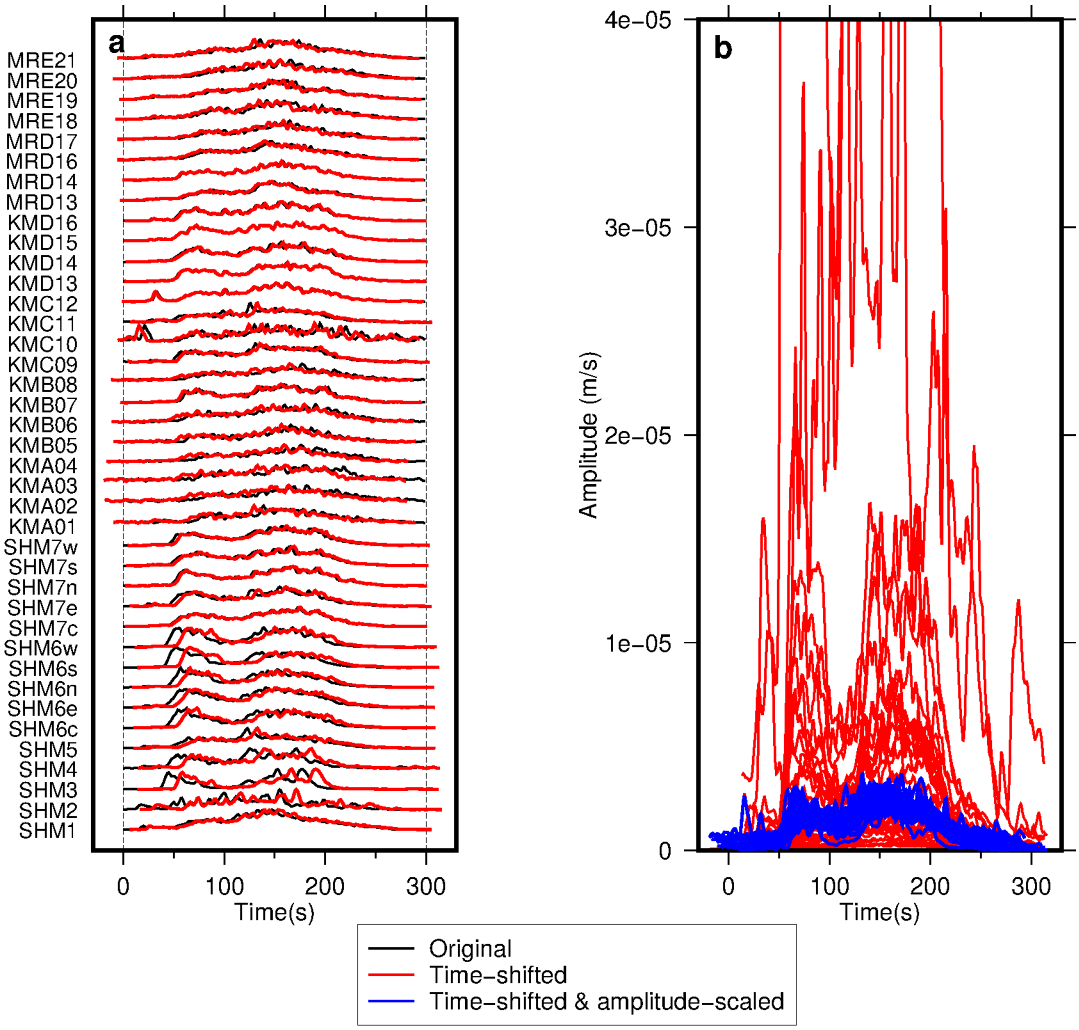

Figure 3. Tremor envelopes of a specific event. (a) Envelopes normalized by the maximum amplitude at each station. The black trace represents the original envelope, and the red trace is time-shifted by t_i^{rel} in Equation (5). The station names are listed along the vertical axis. (b) Envelopes that hold amplitude information. The red trace shows the time-shifted envelopes in the same way as (a), and the blue trace is amplitude-scaled by a_i^{rel} in Equation (7).

3.2. Step 2: Wave propagation-based quality control

The optimization in Step 1 is useful for capturing seismic wave propagation intuitively. In cases where the optimization is successful and not affected by outliers, the relative arrival times and amplitudes exhibit a concentrated pattern when viewed on a map where the center approximates the epicenter, as shown in Fig. 4. We can use this pattern to obtain time–distance and amplitude–distance relationships, which in turn can be used to roughly quantify the propagation speed (i.e., S-wave velocity V_S) or attenuation strength (i.e., quality factor Q_S), respectively.

For a uniform velocity structure throughout the medium, the arrival time t^{syn} is proportional to the propagation distance d:

$$t^{syn} = \frac{d}{V_S}. \tag{9}$$

Thus, V_S can be estimated from the slope of the time–distance plot (Fig. 4c).

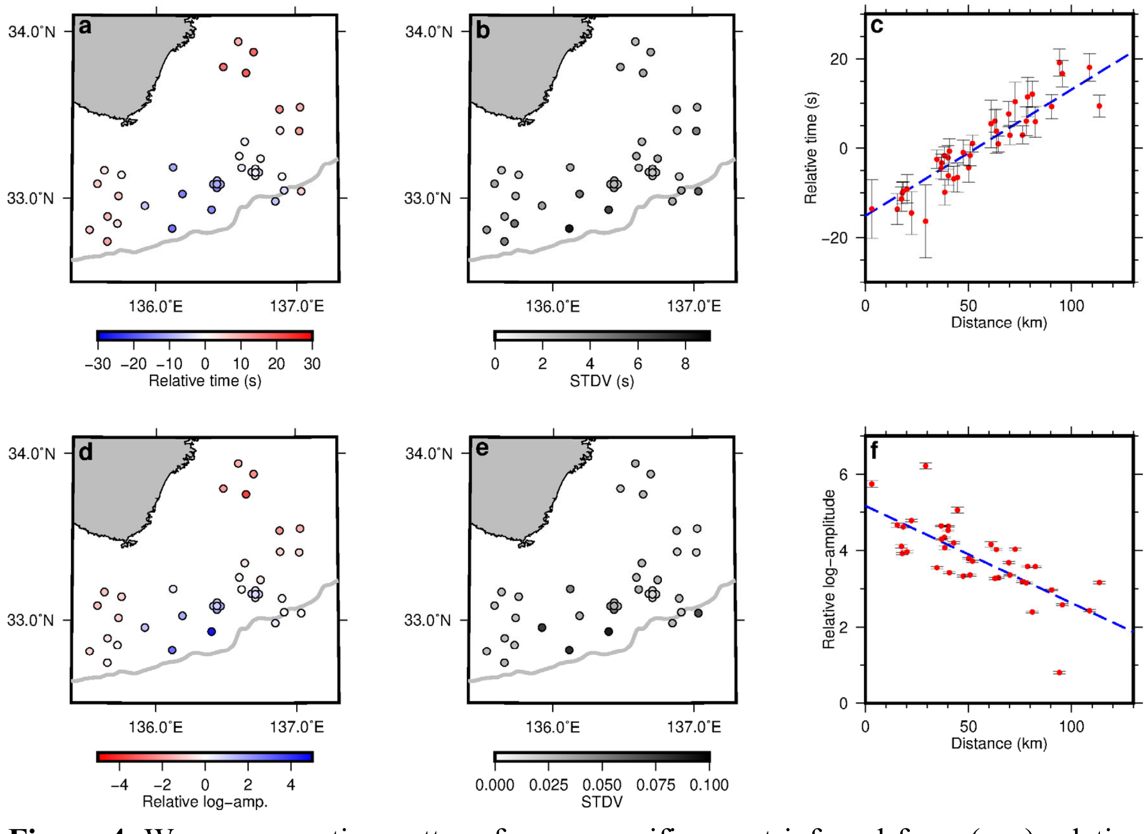

Figure 4. Wave propagation pattern from a specific event inferred from (a–c) relative arrival times and (d–f) relative logarithmic amplitudes. (a) Relative arrival time are shown in map view. The gray line denotes the trench. (b) Standard deviations of the error on the relative arrival times. (c) Relative arrival times plotted against propagation distances. The error bar denotes the standard deviation. The blue dashed line represents a regression line. (d–f) The same as (a–c), but relative logarithmic amplitudes are shown. Note that the effect of geometrical spreading is removed in (f).

The amplitude of a body wave at a propagation distance d is described as

$$a'^{syn} = a_0 \frac{\exp(-Bd)}{d}, \tag{10}$$

$$B = \frac{\pi f}{Q_S V_S}, \tag{11}$$

where a_0 is the source amplitude, f is the representative frequency, and Q_S is the quality factor. Taking the logarithm of Equation (10) leads to

$$a^{syn} \equiv \ln(a'^{syn}) = -Bd + \ln a_0 - \ln d\,. \tag{12}$$

After removing the effect of the geometrical spreading (i.e., removing $-\ln d$ term from Equation (12)), the logarithmic amplitude becomes proportional to the distance. Therefore, we can determine the attenuation strength B from the slope of the amplitude–distance plot (Fig. 4f). Equation (12) neglects the source radiation pattern, but because of the scattering caused by small-scale structural heterogeneities, the radiation pattern would be lost before seismic wave reach stations for the high frequency we use (Takemura et al., 2009).

The well-defined linearity of data in the time– and amplitude–distance plots, such as Fig. 4(c) and (f), can be a reasonable indicator of good-quality events and vice versa. The correlation coefficient between travel time and distance ($C_{time-dist}$) or amplitude and distance ($C_{amp-dist}$) provide useful quantification of such linearity. The high values of $C_{time-dist}$ and $C_{amp-dist}$ guarantees that the source originates from single geographical point.

Furthermore, we propose using the estimated V_S and B from the regression slope as quality control factors, which can pose different conditions than $C_{time-dist}$ and $C_{amp-dist}$. The estimated V_S and B are representative of a broad region where source–receiver paths pass through. Because tectonic tremors always occur in a narrow depth range along the subducting plate boundary (e.g., Audet & Kim, 2016; Saffer & Wallace, 2015), all ray paths most likely propagate through similar depths. Considering that subsurface properties vary less laterally than vertically, the estimated V_S and B values from different events should fall into a narrow and physically reasonable range. Hence, events with outlier V_S and B values may be attributed to ill-optimized datasets or events far isolated from target tremors, such as teleseismic events.

In practice, the propagation distance d is not known before the hypocenter is determined. In this study, we assume that the source is located beneath the station with the maximum relative amplitude. The focal depth is assumed to be 7 km below sea level, considering the depth of the subducting plate of the study area (e.g., Tsuji et al., 2014). This assumption can be replaced by any alternative, depending on the tectonic setting and station geometry. For example, searching for high $C_{time-dist}$ and $C_{amp-dist}$ values on a coarse grid would be a more appropriate option for any setting. The resulting time– and amplitude–distance plots from the assumed source location are then linearly regressed by the least squares method, as shown by the blue dashed lines in Figs 4(c) and (f).

V_S and B values from different events are shown in Fig. 5. We find that the results are relatively concentrated within an area of V_S=2.0–4.0 km/s and B=0.015–0.030 (see the density plot in Fig. 5(c)). Additionally, $C_{time-dist}$ and $C_{amp-dist}$ values tend to high and low, respectively, within this area, showing the increased linearity of time– and amplitude–distance relationships. Based on these features, we selected events with V_S=2.0–4.0 km/s and B=0.015–0.030 as acceptable. These ranges are comparable to those previously estimated for the study area (Akuhara et al., 2020; Yabe et al., 2021), and they correspond to Q_S of 130–520 if a dominant frequency of 5 Hz is assumed. We did not impose any condition on $C_{time-dist}$ and $C_{amp-dist}$ for this study because we found that the selection by V_S and Q_S already requires high $C_{time-dist}$ and $C_{amp-dist}$. Under these criteria, 1296 of the 34,068 events were retained.

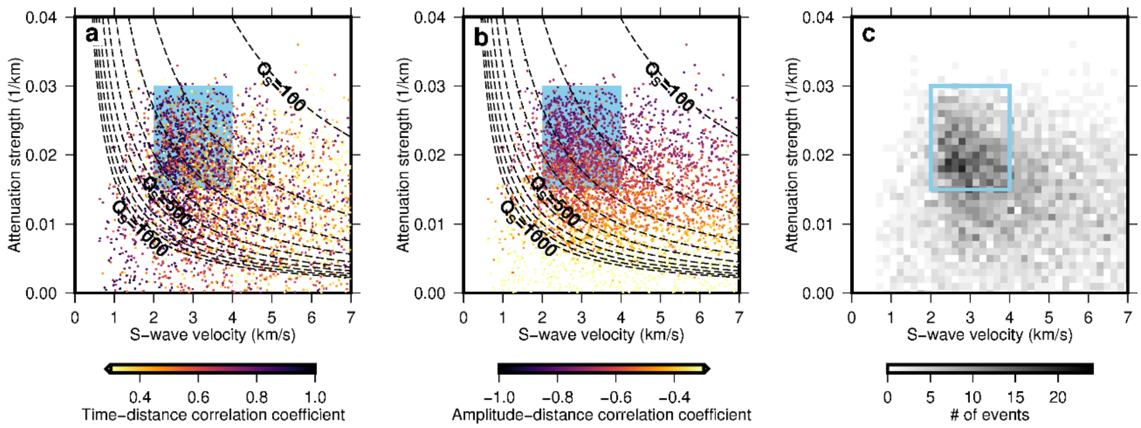

Figure 5. Estimations of the S-wave velocity (V_S) and attenuation strength (B) based on the wave propagation pattern. Each red dot shows the results from different events. The dashed curves are contours of the quality factor (Q_S) from 100 to 1000. A dominant frequency of 5 Hz was assumed. The acceptable ranges of V_S and B are highlighted in pale blue.

It is crucial to note that the above V_S and Q_S estimations are rough based on the simple assumptions on a source location and structures. Still, the above wave propagation-based criteria offer several advantages over conventional non-physics-based quality control factors, such as those based on waveform cross-correlations. In our approach, thresholding values can be selected based on existing knowledge of rock properties (V_S and Q_S) in the study area. In contrast, cross-correlation values have no clear physical interpretation, and their values highly depend on analysis conditions such as frequency ranges and time window lengths. Local site conditions also influence correlation values. In addition, our proposed criteria ensure that the global minimum exists near the propagation center during the hypocenter determination. In contrast, thresholding by cross-correlation cannot guarantee a global minimum even if cross-correlation values are high. This can be illustrated by teleseismic events, where waveforms exhibit high coherency among stations, but no global minimum can be identified.

3.3. Step 3: Bayesian inversion

In Step 3, we adopt a Bayesian interface to invert the relative arrival times and logarithmic amplitudes jointly for the hypocenters $(x_j, y_j, z_j; j = 1, \cdots, N_{evt})$, delay factor for each station ($\tau_i^{sta}; i = 1, \cdots, N_{sta}$), amplification factor for each station ($\alpha_i^{sta}; i = 1, \cdots N_{sta}$), S-wave velocity ($V_S$), and quality factor ($Q_S$). Here, N_{sta} and N_{evt} represent the numbers of stations and events, respectively. The delay and amplification factors are used to account for the local site effects caused by seafloor sediment beneath the stations. We assumed uniform structures for the S-wave velocity and attenuation for simplicity. These model parameters are denoted by $\boldsymbol{m}$ hereafter.

The relative arrival times and logarithmic amplitudes and the associated uncertainties given by Equations (5)–(8) are used as inputs for the inversion. To distinguish different events, we append a subscript to the notation of these inputs. For instance, t_{ij}^{rel} has the same meaning as t_i^{rel} in Equation (5) but is for the jth event. a_{ij}^{rel}, σ_{ij}^{time}, and σ_{ij}^{amp} are defined in a similar manner. Furthermore, the following vector notation is used:

$$\boldsymbol{d}^{time} = \left(t_{11}^{rel} \cdots t_{ij}^{rel} \cdots t_{N_{sta}N_{evt}}^{rel}\right)^{\top}, \tag{13}$$

$$\boldsymbol{d}^{amp} = \left(a_{11}^{rel} \cdots a_{ij}^{rel} \cdots a_{N_{sta}N_{evt}}^{rel}\right)^{\top}, \tag{14}$$

$$\boldsymbol{\sigma}^{time} = \left(\sigma_{11}^{time} \cdots \sigma_{ij}^{time} \cdots \sigma_{N_{sta}N_{evt}}^{time}\right)^{\top}, \tag{15}$$

$$\boldsymbol{\sigma}^{amp} = \left(\sigma_{11}^{amp} \cdots \sigma_{ij}^{amp} \cdots \sigma_{N_{sta}N_{evt}}^{amp}\right)^{\top}. \tag{16}$$

The posterior probability of the model parameters $(\boldsymbol{m})$ can be written as

$$\begin{aligned} &P\left(\boldsymbol{m} \middle| \boldsymbol{d}^{time}, \boldsymbol{d}^{amp}; \boldsymbol{\sigma}^{time}, \boldsymbol{\sigma}^{amp}\right) \\ &= CP(\boldsymbol{m})P\left(\boldsymbol{d}^{time} \middle| \boldsymbol{m}; \boldsymbol{\sigma}^{time}\right)P(\boldsymbol{d}^{amp} | \boldsymbol{m}; \boldsymbol{\sigma}^{amp}) \end{aligned} \tag{17}$$

where $P(\boldsymbol{m})$ is the prior probability; $P(\boldsymbol{d}^{time}|\boldsymbol{m};\boldsymbol{\sigma}^{time})$ and $P(\boldsymbol{d}^{amp}|\boldsymbol{m};\boldsymbol{\sigma}^{amp})$ are the likelihoods regarding the time and amplitude data, respectively; and C is a normalization constant. Direct computation of Equation (17) is infeasible because the normalization constant involves integration over the entire model space. However, the posterior probability can be estimated via probabilistic sampling, such as with the MCMC algorithm.

We assumed a Gaussian distribution for the prior probability of the horizontal locations, station correction terms, S-wave velocity, and quality factor:

$$P(\theta) = \frac{1}{\sqrt{2\pi {\sigma_{prior}^{\theta}}^2}} \exp\left[-\frac{\left(\theta - \mu_{prior}^{\theta}\right)^2}{2{\sigma_{prior}^{\theta}}^2}\right], \tag{18}$$

where μ_{prior}^{θ} and σ_{prior}^{θ} are the mean and standard deviation, respectively, and θ is either x_j, y_j, τ_i^{sta}, α_i^{sta}, V_S, or Q_S.

We adopted Rayleigh distribution for event depths:

$$P(z_j) = \frac{z_j - z_0}{{\sigma_{prior}^{z_j}}^2} \exp\left(-\frac{\left(z_j - z_0\right)^2}{2{\sigma_{prior}^{z_j}}^2}\right). \tag{19}$$

Here, z_0 is added to the usual formulation of the Rayleigh distribution. Without this term, the Rayleigh distribution is defined for positive values (i.e., $z > 0$). Adding z_0 changes the domain to $z > z_0$. Introducing z_0 may be useful for prohibiting hypocenters located above the seafloor, although we found that it did not affect the results significantly. For z_0 = 0 km and $\sigma_{prior}^{z_j}$ = 10 km, the 95% confidence interval of the Rayleigh distribution is 2.3– 27.2 km, wide enough to be deemed as noninformative for the study area.

Table 1 presents the selected parameter values for these priors. Note that the selected parameter values have a minimal impact on the posterior probability except in cases where extremely narrow ranges are employed. This insensitivity aligns with theoretical expectations: as the amount of data increases, the weight of the prior probability on the posterior probability exponentially decays. This behavior should not be confused with the regularization often used in geophysical inversion, which suppresses solutions that deviate from the initial model. In such analyses, the regularization weight is determined ad hoc regardless of the amount of data.

Table 1. Parameter selection for the prior probability

Description	Notation	Values used

Event horizontal locations (Equation (18))	$\mu_{prior}^{x_j}, \mu_{prior}^{y_j}$	Station location showing the maximum amplitude
	$\sigma_{prior}^{x_j}, \sigma_{prior}^{y_j}$	30 km
Event depth (Equation (19))	$\sigma_{prior}^{z_j}$	10 km
	z_0	0 km
Delay factor (Equation (18))	$\mu_{prior}^{\tau_i}$	0 s
	$\sigma_{prior}^{\tau_i}$	0.5 s
Amplification factor (Equation (18))	$\mu_{prior}^{\alpha_i}$	0 (= 0 dB)
	$\sigma_{prior}^{\alpha_i}$	0.02 (= 0.09 dB)
S-wave velocity (Equation (18))	$\mu_{prior}^{V_S}$	3.0 km/s
	$\sigma_{prior}^{V_S}$	1.0 km/s
Quality factor (Equation (18))	$\mu_{prior}^{Q_S}$	250
	$\sigma_{prior}^{Q_S}$	100

The likelihood function for the arrival time can be defined as follows, assuming that the data errors are normally distributed without covariance:

$$P(\boldsymbol{d}^{time}|\boldsymbol{m};\ \boldsymbol{\sigma}^{time}) = \prod_{i=1}^{N_{sta}} \prod_{j=1}^{N_{evt}} \frac{1}{\sqrt{2\pi {\sigma_{ij}^{time}}^2}} \exp\left\{-\frac{\left[t_{ij}^{syn}(x_i, y_i, z_i, V_S) + \tau_i^{sta} - \tau_j^{evt} - t_{ij}^{rel}\right]^2}{2{\sigma_{ij}^{time}}^2}\right\}, \quad (20)$$

where t_{ij}^{syn} is the synthetic travel time based on the hypocenter and S-wave velocity, and the subscripts i and j correspond to station and event indices, respectively. The synthetic travel time is added by τ_i^{sta} to account for the time delay due to local site conditions.

Note that the synthetic travel time t_{ij}^{syn}, which is relative to the origin time, cannot be directly compared to the observed relative arrival times t_{ij}^{rel}. These relative arrival times are subtracted by the station average, as per the regularization condition described in Equation (4)). To enable a meaningful comparison, Equation (20), introduces an adjustment by subtracting an event-specific term τ_j^{evt}. Ideally, τ_j^{evt} is equal to the average of the synthetic travel times across all stations, the same amount as subtracted by the regularization condition. However, in practice, τ_j^{evt} is unknown because it can deviate from the ideal value with the presence of measurement errors. We therefore incorporate τ_j^{evt} as a model parameter, and set it to the MLE:

$$\tau_j^{evt} = \frac{\sum_{i=1}^{N_{sta}} \frac{t_{ij}^{syn}(x_i, y_i, z_i, V_S) + \tau_i^{sta} - t_{ij}^{rel}}{\sigma_{ij}^{time^2}}}{\sum_{i=1}^{N_{sta}} \frac{1}{\sigma_{ij}^{time^2}}}. \tag{21}$$

Note that Equation (21) corresponds to the averaged residual over stations weighted by data variance, which can be derived from $\frac{\partial \mathcal{L}^{time}}{\partial \tau_j^{evt}} = 0$.

Similar equations hold for the logarithmic amplitudes:

$$P(\boldsymbol{d}^{amp}|\boldsymbol{m};\, \boldsymbol{\sigma}^{amp}) = \prod_{i=1}^{N_{sta}} \prod_{j=1}^{N_{evt}} \frac{1}{\sqrt{2\pi\sigma_{ij}^{amp^2}}} \exp\left\{ -\frac{\left[a_{ij}^{syn}(x_i, y_i, z_i, V_S, Q_S) + \alpha_i^{sta} - \alpha_j^{evt} - a_{ij}^{rel}\right]^2}{2\sigma_{ij}^{amp^2}} \right\}, \tag{22}$$

$$\alpha_j^{evt} = \frac{\sum_{i=1}^{N_{sta}} \frac{a_{ij}^{syn}(x_i, y_i, z_i, V_S, Q_S) + \alpha_i^{sta} - a_{ij}^{rel}}{\sigma_{ij}^{amp^2}}}{\sum_{i=1}^{N_{sta}} \frac{1}{\sigma_{ij}^{amp^2}}}, \tag{23}$$

where a_{ij}^{syn} is synthetic logarithmic amplitude, and α_j^{evt} is the event-specific term to be set to the MLE, in accordance with Equation (23). Notably, the term for source amplitude a_0 is canceled out when Equation (12) is substituted into Equations (22) and (23), which eliminates the need to estimate the source amplitude beforehand.

Based on Equations (17)–(23), we can use the MCMC algorithm to sample the posterior probability. At each iteration, one of the model parameters $\boldsymbol{m}$ is perturbed randomly, where the amount of perturbation is drawn from a zero-mean Gaussian distribution with a standard deviation, as given in Table 2. We chose values for these perturbation parameters by trial and errors, referring to the likelihood evolution over iterations. The perturbed model parameters $\boldsymbol{m'}$ is accepted in accordance with a probability α described by the Metropolis–Hastings criteria (Hastings, 1970; Metropolis et al., 1953):

$$\alpha = \min\left[1, \frac{P(\boldsymbol{m'})}{P(\boldsymbol{m})} \cdot \frac{P(\boldsymbol{d}^{time}|\boldsymbol{m'};\boldsymbol{\sigma}^{time})}{P(\boldsymbol{d}^{time}|\boldsymbol{m};\boldsymbol{\sigma}^{time})} \cdot \frac{P(\boldsymbol{d}^{amp}|\boldsymbol{m'};\boldsymbol{\sigma}^{amp})}{P(\boldsymbol{d}^{amp}|\boldsymbol{m};\boldsymbol{\sigma}^{amp})}\right]. \tag{24}$$

Table 2. Random walk parameters for the MCMC algorithm

Parameter to be perturbed	Standard deviation used to retrieve the perturbation amount
x_j	2.0 km
y_j	2.0 km
z_j	0.4 km
τ_i^{sta}	0.03 s
α_j^{sta}	0.005 (= 0.022 dB)
V_S	0.2 km/s
Q_S	5

We performed 8 million iterations, with the first 4 million iterations treated as a burn-in period. The sampled model parameters were saved at every 4000 iterations during the second 4 million iterations. We ran 100 chains of the MCMC algorithm in parallel and allowed them to mutually interact by using a parallel tempering technique for an efficient global search (Geyer, 1991; Sambridge, 2014). In this technique, the likelihood-ratio in the acceptance criteria is adjusted based on temperature parameter, denoted as T:

$$\alpha' = \min\left[1, \frac{P(\boldsymbol{m}')}{P(\boldsymbol{m})} \cdot \left\{\frac{P(\boldsymbol{d}^{time}|\boldsymbol{m}'; \boldsymbol{\sigma}^{time})}{P(\boldsymbol{d}^{time}|\boldsymbol{m}; \boldsymbol{\sigma}^{time})} \cdot \frac{P(\boldsymbol{d}^{amp}|\boldsymbol{m}'; \boldsymbol{\sigma}^{amp})}{P(\boldsymbol{d}^{amp}|\boldsymbol{m}; \boldsymbol{\sigma}^{amp})}\right\}^{\frac{1}{T}}\right]. \tag{25}$$

With this modification, higher-temperature chains have more chance to accept new samples, leading to random sampling more globally. These temperatures are proposed to be swapped between a chain pair randomly selected, and the proposal is accepted with a certain probability to maintain the detailed balance (Sambridge, 2014). Through this temperature swap, non-tempered ($T = 1$) chains, which is used to calculate the posterior probability, can benefit from global sampling accomplished by higher-temperature chains. We set T=1 for 20 Markov chains, while the remaining 80 chains were assigned temperatures between 1 and 200. The temperature swap was proposed 10 times per iteration.

4. Results and discussion

4.1. Inversion results

We applied the above inversion method of Step 3 to the amplitude and time data from the 1296 events that passed the quality control in Step 2. The likelihood almost monotonically increased with the number of iterations and converged within the burn-in period (Fig. 6a, black dots), which suggests that model parameters sampled after the burn-in period can simulate the posterior probability. To evaluate the effect of the parallel tempering scheme, we conducted a parallel inversion analysis using 100 MCMC chains but without tempering. As a result, the likelihood increased at a slower pace than the tempered analysis (Fig. 6a, gray dots). Only ~10% of chains reached the same likelihood level as the tempering method at the 600,000th iteration (Fig. 6b), highlighting the effective global search offered by the parallel tempering method.

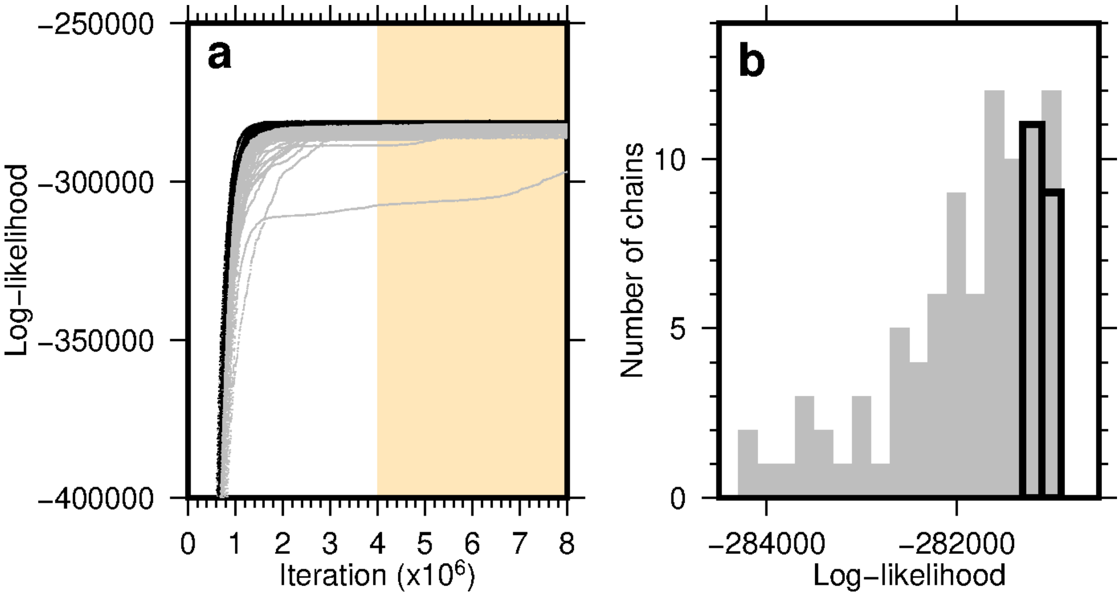

Figure 6. (a) Likelihood evolution. Black dots show the likelihood of MCMC samples by 20 non-tempered chains. The underlying gray dots show the results of independent inversion without parallel tempering for which 100 non-tempered chains were employed. The yellow-shaded area highlights iterations after the burn-in period. (b) Histograms of the likelihood sampled by non-tempered MCMC chains at the 600,000th iteration. The black and gray histograms show the results with and without the tempering scheme, respectively.

After conducting the inversion analysis, we obtained 20,000 MCMC samples of model parameters. For most events, the posterior probability constructed by the MCMC samples exhibit monotonous peak for hypocenter parameters (i.e., x_j, y_j, and z_j), as some examples are shown in Fig. S2. From the MCMC samples, we calculated the median and 95% confidence intervals as statistical measures for each model parameter. Then, to prevent duplication of events between successive and overlapped 300-s time segments, we discarded the results from the later time segment if they shared a common hypocenter.

Specifically, if the median hypocenter fell within the 95% interval of the opponent, we considered them duplicates. Following this process, we retained 1208 unique events.

The inversion results are summarized in Fig. 7. The epicenters, which we defined as the median of the MCMC samples, are tightly clustered in the map view. The 95% confidence interval of horizontal location is typically <5 km in the east–west direction (blue histogram in Fig. 7a) and <7 km in the north-south direction (blue histogram in Fig. 7b). The confidence intervals are slightly less in the east–west direction than in the north–south direction because the seismic network geometry is elongated in the east-west direction and variation of the subsurface structures is relatively gentle in the trench-parallel direction. The typical confidence interval for event depths are < 10 km (blue histogram in Fig. 7c). Unfortunately, the vertical uncertainties are insufficient to discuss the source faults of the tectonic tremors considering the subduction depth of ~6–8 km. Because of this loose constraint on the depth, some hypocenters are located above the seafloor. We may explicitly prohibit such unlikely solutions by increasing z_0 in Equation (19), although this change had almost no influence on the horizontal locations (Fig. S3). We also found that consistent results were obtained from the non-tempered analysis (Fig. S4). However, because of the poor convergence, the non-tempered analysis produced more uncertain events with 95% intervals greater than 10 km than the tempered analysis (Fig. S5).

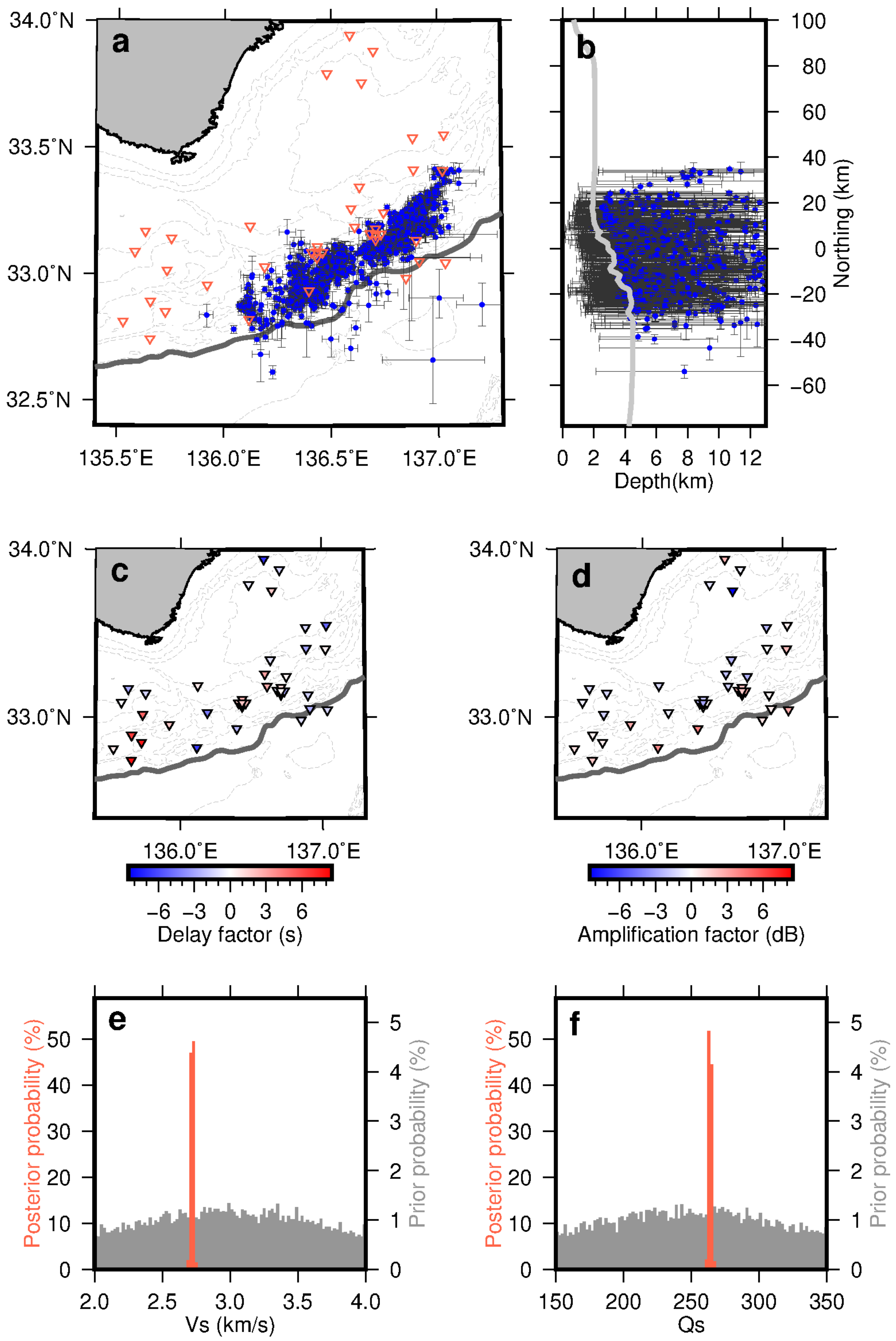

Figure 7. Inversion results. (a, b) Hypocenters. Each blue dot shows the median hypocenter of the MCMC samples for each event. The error bars represent the 95% confidence interval derived from MCMC samples. The inverted triangles are seismic stations. The thick gray line in (a) represents the trench. The thick gray line in (b) represents the bathymetry along 136.5°E. (c, d) Median estimates of (c) delay factors

and (d) amplification factors of the MCMC samples. (e, f) Probability distributions of the (e) S-wave velocity and (f) quality factor. Red and gray histograms show the posterior and prior distributions, respectively.

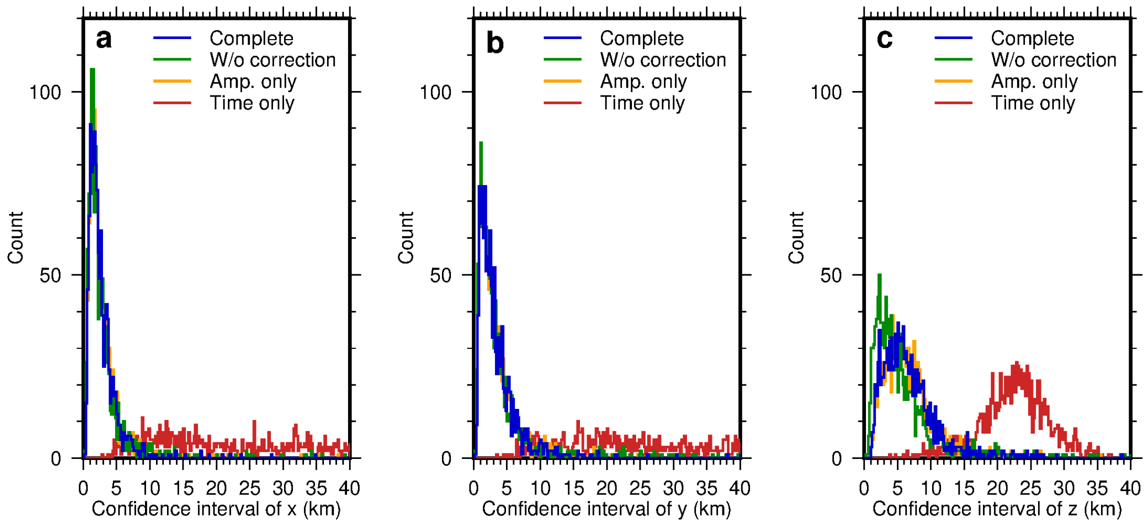

Figure 8. Histograms of the hypocenter uncertainties (i.e., the range of 95% confidence interval) in the (a) east–west, (b) north–south, and (c) vertical directions. The differently colored histograms show the hypocenter uncertainties from different inversion settings: the complete case (blue), without correction terms (green), amplitude data only (orange), and time data only (red).

The median values of the delay and amplification factors range from -7.0 to 8.0 s and from -8.6 to 4.2 dB, respectively (Figs 7c and d). These ranges are significantly larger than the 95% confidence interval obtained for individual stations (Fig. S6); therefore, the spatial pattern seen in Figs 7(c) and (d) is reliable. Overall, these values exhibit a smooth lateral variation, with stations near the trench experiencing earlier arrivals and a more significant amplification than predicted. The thinner accretionary prism near the trench likely explains the early arrivals, which allows seismic waves to travel through the subducted crust at faster velocities. In addition, the significant amplification at the trench is reasonable because the trench-fill sediments are less consolidated than the landward accretionary prism (Tsuji et al., 2011). Station MRE20 exceptionally shows a delayed arrival near the trench. Because this station is separated from the majority of events, this delayed arrival may account for the structural heterogeneities in the trench-parallel direction.

The posterior probabilities of the S-wave velocity and quality factor have narrow peaks, with mean values of 2.72 km/s and 263, respectively (Figs 7e and f). These values correspond to an attenuation strength of 2.20×10^{-2} km^{-1}, and they are consistent with those obtained from the regression analysis (Fig. 5). The S-wave velocity of 2.72 km/s is somewhat slower than that reported for the oceanic crust of this region (>3 km/s) but is comparable to the velocity of the underthrust sediment immediately above the crust (Akuhara et al., 2020). Yabe et al. (2021) independently estimated the attenuation strength of this region as a function of the hypocentral distance by using the seismic amplitudes of tectonic tremors that occurred in different periods, and their results are mostly consistent with our estimations.

4.2. Contributions of each factor

The proposed method offers several improvements compared to conventional analyses. For better understanding of its advantages, the contributions of different factors need to be considered, and hence we performed inversion under different settings (Fig. 9). Fig. 9(a) shows the inversion results from Fig. 7 (i.e., complete case). Fig. 9(b) shows the inversion results when the delay and amplification factors are excluded by setting their values to zero (i.e., without-correction case). Fig. 9(c) shows the inversion results when the relative arrival time data are excluded and only the amplitude information was used (i.e., amplitude-only case). In this case, the amplification and quality factors are solved while the S-wave velocity V_S is fixed at 3.0 km/s. This fixed V_S value affects the estimation of Q_S through Equation (11) but not the other parameters. Fig. 9(d) shows the inversion results when only the time data are used with the S-wave velocity and delay factors solved (i.e., time-only case). This case does not involve the attenuation parameter.

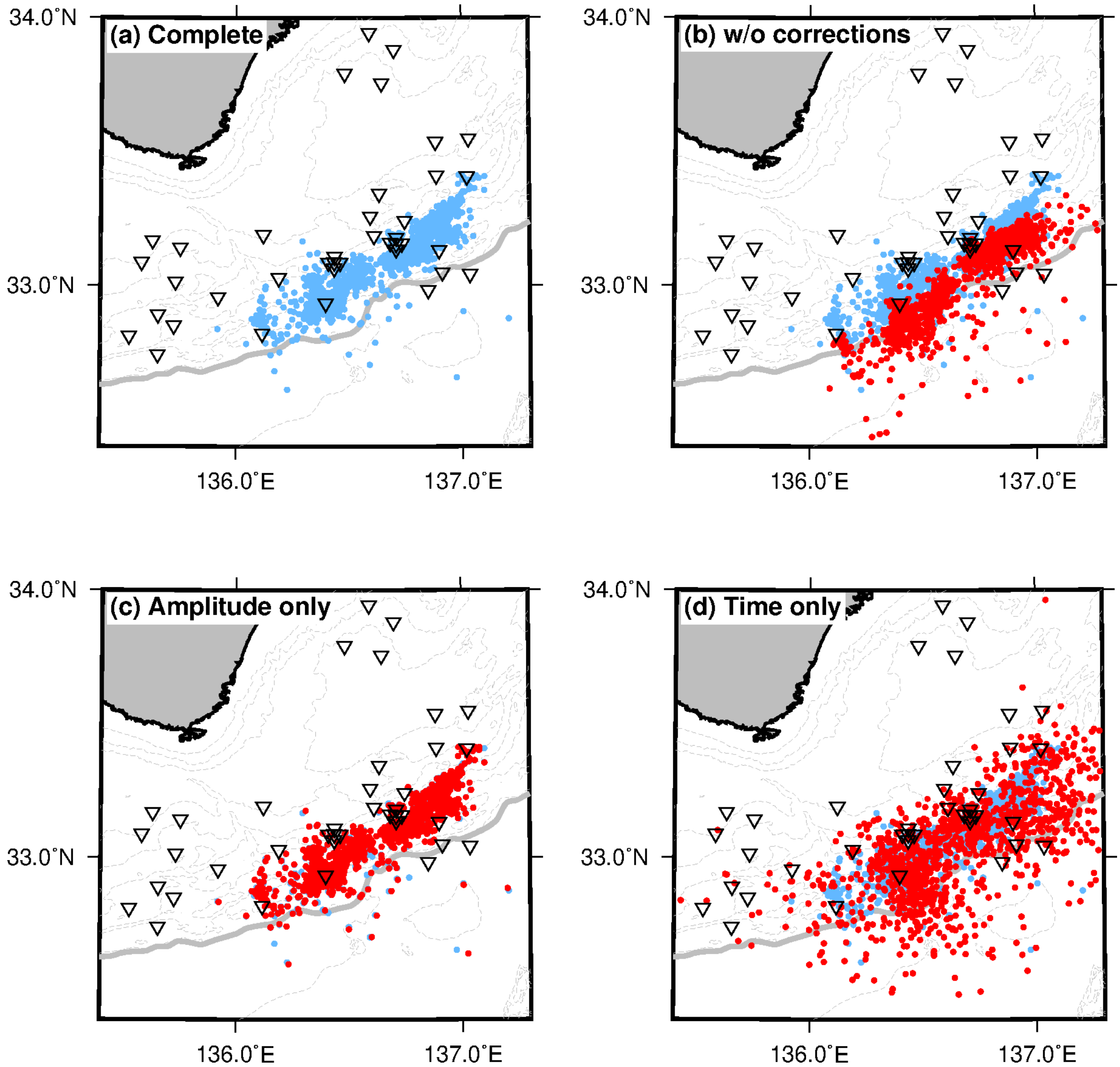

Figure 9. Inversion results under different settings: (a) complete, (b) without corrections (i.e., amplification and delay factors), (c) amplitude data only, and (d) time data only. The pale-blue dots are hypocenters (i.e., median values of the MCMC samples) in the complete case. The red dots are the resultant hypocenters in the other cases. The inverted triangles are seismic stations. The gray line represents the trench.

In the without-correction case, the hypocenters are systemically located further seaward than in the complete case. Although we do not know the true hypocenters, the without-correction case shifts many events seaward of the trench, which is highly unlikely. We conjecture that adding correction factors accounts for structural heterogeneities in the along-dip direction, which helps correct this artificial shift. The seaward shift is ~10 km on the western side, where station coverage is relatively limited. These shifts are greater than the uncertainties of the hypocenters shown in Figs 8(a) and (b). Failing to consider these corrections can significantly bias the results and lead to misinterpretation.

The time-only case suffers from a greater uncertainty for the hypocenters than the amplitude-only case (Fig. 8). The hypocenters are more scattered in space in the time-only case (Fig. 9d) whereas they are similar to the complete case in the amplitude-only case (Fig. 9c). These discrepancies can be attributed to the considerable uncertainty in the relative arrival times, which can be quantitatively understood from the distance plots in Figs 4(c) and (f). For example, the typical error in the relative arrival time σ^{time} can be read as 5 s from Fig. 4(c) while the typical error in the relative amplitude σ^{amp} can be read as 0.05 from Fig. 4(f). The typical errors in epicenter can then be calculated as $\sigma^{time} \cdot (\partial T/\partial d)^{-1}$ or $\sigma^{amp} \cdot (\partial A/\partial d)^{-1}$, where $\partial T/\partial d$ and $\partial A/\partial d$ represent the slopes of the regression lines in the time–distance and amplitude–distance plots, respectively. If $\partial T/\partial d$ is 0.3 $\mathrm{s} \cdot \mathrm{km}^{-1}$ and $\partial A/\partial d$ is 0.03, the error for the epicenter is 17 km using time data and 1.7 km using the amplitude data, which indicates a difference of an order of magnitude.

The large uncertainties in the relative arrival times originates from the inconsistencies in arrival time differences among station pairs. Takemura et al. (2020) showed that a slow and heterogeneous accretionary prism complicates tremor waveforms as they propagate over longer distances. Measuring arrival time difference between stations at greater distances are more susceptible to this waveform distortion, which can increase the inconsistency (see envelopes in Fig. 3(a), where envelopes from closely located stations, e.g., KMA01–KMA02, show a higher degree of similarity than stations separated by greater distances, e.g., SHM1–SHM7c). A common strategy to mitigate this issue is to limit station pairs to those with shorter distances or high coherencies. However, such data selection is often based on subjective criteria.

Our results demonstrate the superiority of amplitude data for tectonic tremor location because it can pose tight constraints on hypocenters without any ad hoc selection of data. Challenges associated with using amplitude data may include difficulties with estimating the source amplitude, attenuation strength, and local site effects beforehand. However, the proposed inversion approach eliminates the need for these prerequisite processes.

4.3. Spatiotemporal evolution of tremors

The proposed method provides well-constrained epicenters with typical confidence interval of <7 km. This allows the spatiotemporal evolution of the tremor activity to be discussed in detail. As shown in Fig. 10(a), the located tremors can be divided into three main groups (A–C). The Groups A and B are separated by ~5 km, while the Groups B and

C by ~10 km.

Fig. 10(b) shows that the tremor episode originates from the eastern end of Group A and then migrates southwestward, parallel to the trench, at a speed of ~3 km/day (referred to as Phase i). Such migration of tremors has been commonly observed worldwide, and it is thought to reflect an undergoing slow slip event. Immediately after the migration front reaches the western end of Group A, tremor activity in Group B starts at the eastern side (Phase ii), followed by backward migration within Group A at a speed of ~17 km/day (Phase iii). After this backward migration ceases, bilateral migration both southwestward and northeastward take place at different asymmetric propagation speed (Phases iv–vii). The southwestward migration seems to activate tremors in Group C (Phase v), and the relatively slow propagation at ~2 km/day suddenly speeds up to ~13 km/day when the migration front approaches Group A (Phase vii). This fast migration lasted for 3 days. Then, after a quiescence period of about 1 day, relatively small-scale activity occurs in the eastern part of Group B (Phase viii). The observed spatiotemporal evolution of the tremors is roughly consistent with that described by Ogiso & Tamaribuchi (2022), who used amplitude data from DONET stations to determine tremor locations (Fig. S7).

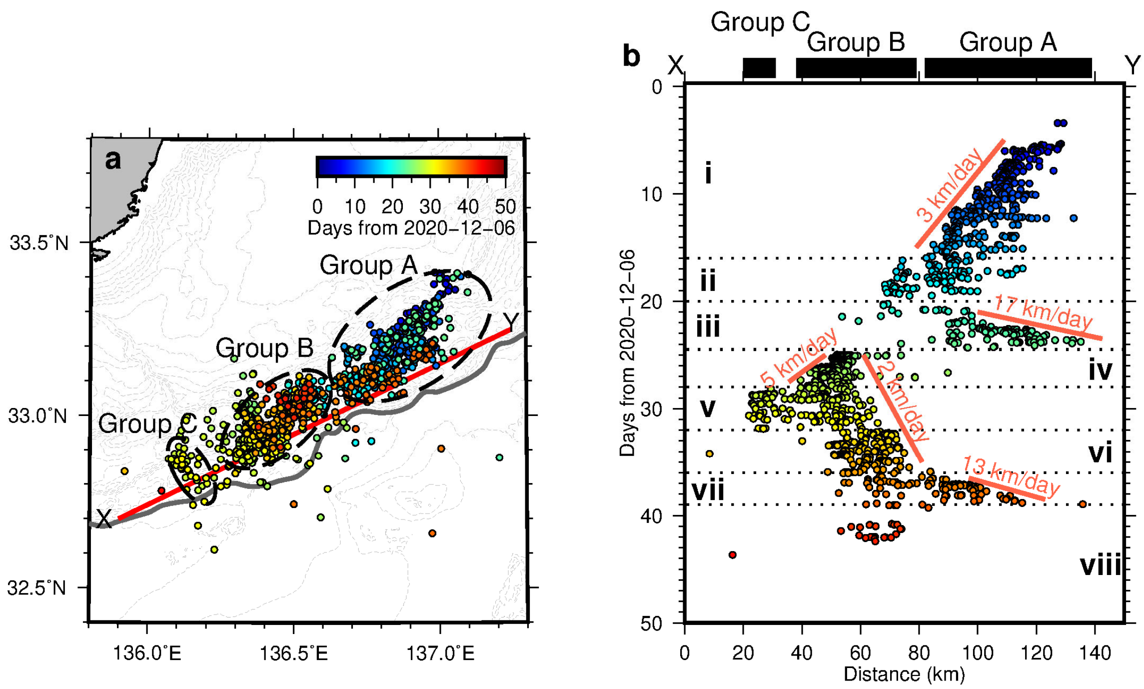

Figure 10. Spatiotemporal evolution of tremors. (a) Map view of tremor epicenters with colors corresponding to days of the study period. The gray line represents the trench. (b) Temporal evolution of tremors projected along the X–Y profile (red line in (a)). The color

notation corresponds to that in (a). The orange inclined lines delineate trench-parallel migration of tremors. Note that only the first 50 days are shown because this study detected no tremor after this period.

Our use of the stochastic sampling technique facilitates the exploration of subtle features within the tremor patterns while minimizing the risk of misinterpretation. For example, we can calculate the probability that any tremor epicenter is located at a particular geographical point (x, y) as $p_{any}(x, y) = 1 - \prod_{i=1}^{N_{evt}}[1 - p_i(x, y)]$, where $p_i(x, y)$ denotes the marginalized posterior probability for the i th event epicenter (x_i, y_i). Visualizing this probability allows us to identify fine-scale spatial patterns of tremors without being disturbed by events with large uncertainties because such uncertain events have a limited impact on p_{any}.

Fig. 11 shows the obtained map of p_{any}, clearly highlighting the separations between Groups A–C. Furthermore, the probabilistic map reveals striations of tremors that are difficult to deduce from the standard epicenter map in Fig. 10(a). The epicenters of groups B and C exhibit lineaments oriented toward the direction perpendicular to the trench. These lineaments are identifiable throughout Phases iv–vi. The trench-normal striations may originate from the past subduction of rough topography, similar to what has been interpreted for deep tectonic tremors in southwestern Japan (Ide, 2010). For Group A, such trench-normal striations are not evident. Instead, during Phases iii and vii characterized by relatively high-speed migration (>10 km/day), the epicenters tend to align in a trench-parallel direction. This trench-parallel features might be linked to the topography of the decollement (Hashimoto et al., 2022), although a more detailed analysis is left for our future study.

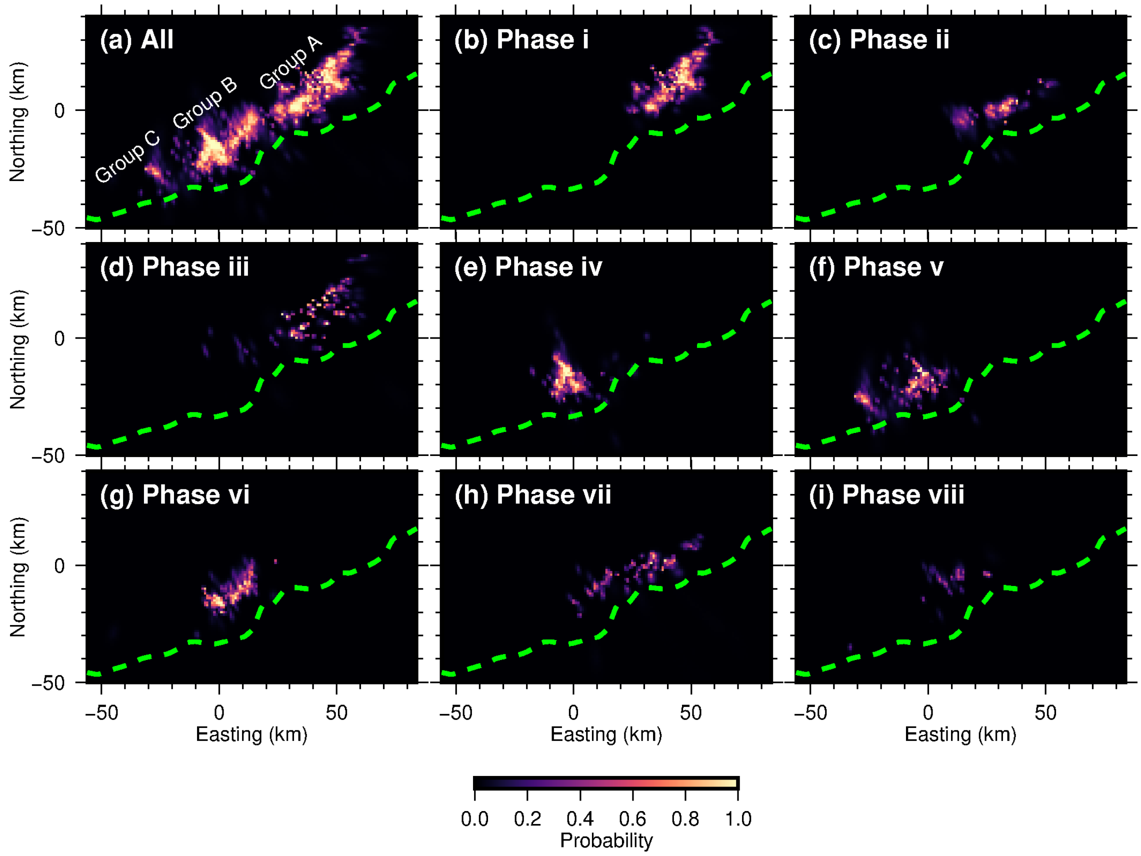

Figure 11. Probability of at least one tremor being located within a 1 km × 1 km cell. (a) The probability calculated for the entire observation period. (b–i) The probability calculated using events within a specific period defined in Fig. 10(b). The green dashed line represents the trench.

5. Conclusions and future perspectives

We proposed a novel three-step method for locating tectonic tremors that employs the optimization of time- and amplitude-difference data, quality control via rough estimates of the propagation speed and attenuation strength, and joint inversion of multiple events using the MCMC algorithm. The proposed method eliminates the need for subjective tuning of data weights and avoids relying on prior knowledge of subsurface structures, local site effects, and source amplitudes. Although some subjective choices are still necessary to set quality control thresholds for Q_S and B, these choices do not distort the uncertainty estimation. When applied to real data, the proposed method demonstrated its effectiveness. Appropriately weighting data by their uncertainties was shown to mitigate the undesirable influence of low-quality data (Figs 9c and d), and the correction terms for time delay and amplification effects from local site conditions significantly reduced systematic biases (Fig. 9b). Furthermore, using a probabilistic mapping technique allowed us to better comprehend the detailed patterns in locations of tectonic tremors (Fig. 11). Specifically, we were able to identify striations in the tremor sources. This provides valuable insights into the underlying structural factors that favor tremor activities.

The proposed method still has room for improvement. One of the main assumptions is that the subsurface structures for V_S and Q_S are uniform, which can potentially impact the results. The difference between the assumed and real structures would be accounted for by time delay and amplification factors. Hence, using more sophisticated correction factors, such as source-specific corrections, may help address this bias (e.g., Lomax & Savvaidis, 2022; Richards-Dinger & Shearer, 2000). Alternatively, the spatial variation of V_S and Q_S can be solved as unknown parameters, similar to a tomographic approach. The narrow peaks observed in the posterior probabilities (Figs7e and f) suggest that such an attempt could be promising.

One aspect that we did not discuss in the present study is the criteria for detecting tectonic tremors. In this study, we used the 98th percentile of the histograms of cross-correlation values as a threshold, which was an arbitrary choice. However, the propagation-based quality control in Step 2 of the proposed method provides an alternative approach to detecting tremors. Specifically, applying the selection criteria based on V_S and B to all time segments not prescreened by cross-correlation coefficients can incorporate wave-propagation information into the detection process, which would increase its robustness compared to relying solely on waveform similarities. However, one drawback of this wave-propagation-based detection is that it requires high signal-to-noise ratios across the entire seismic network. Solving this problem is left for future work, but using such an objective detection method would help illuminate other important aspects of tectonic tremors, such as the frequency distribution (e.g., Nakano et al., 2019).

While obtaining the detailed features of tremor locations is the key to understanding the physical processes behind them, it is particularly challenging for offshore regions, where the accurate location of tremors is hindered by strong heterogeneities in the shallow sedimentary structure. Our results demonstrated that our proposed method is applicable even to such challenging ocean-bottom data. Tectonic tremors that occur in shallow subduction zones remain underexplored. We believe that applying our proposed technique can shed new light on these phenomena.

Appendix A. Maximum likelihood estimation for the amplitude ratio

Consider two waveforms $u_1(t)$ and $u_2(t)$ mutually equivalent except for their normalization constants:

$$u_1(t) - A_{12} \cdot u_2(t) = \varepsilon(t), \qquad (A1)$$

where A_{12} is a time-invariant constant representing an amplitude ratio and $\varepsilon(t)$ is noise contribution. If the noise is assumed to obey a Gaussian distribution (i.e., $\varepsilon(t) \sim N(0, \sigma^2)$) and to be temporarily independent, the likelihood of the amplitude ratio $\mathcal{L}(A_{12})$ can be expressed as

$$\mathcal{L}(A_{12}) = \frac{1}{(2\pi\sigma^2)^{\frac{N}{2}}} \prod_{t=1}^{N} \exp\left(-\frac{\left(u_1(t) - A_{12} \cdot u_2(t)\right)^2}{2\sigma^2}\right). \qquad (A2)$$

Maximizing Equation (A2) corresponds to minimizing the sum of the exponents, which can be achieved under the following condition:

$$\frac{\partial}{\partial A_{12}} \sum_{t=1}^{N} \left(u_1(t) - A_{12} \cdot u_2(t)\right)^2 = 0. \qquad (A3)$$

The left-hand side of Equation (A3) can be rearranged as follows:

$$\frac{\partial}{\partial A_{12}} \sum_{t=1}^{N} \left(u_1(t) - A_{12} \cdot u_2(t)\right)^2 = -2\left(\sum_{t=1}^{N} u_1(t)u_2(t)\right) + 2A_{12}\left(\sum_{t=1}^{N} u_2(t)u_2(t)\right). (A4)$$

From Equations (A3) and (A4), we obtain the MLE of the amplitude ratio:

$$A_{12}^{MLE} = \sum_{t=1}^{N} u_1(t)u_2(t) \Bigg/ \sum_{t=1}^{N} u_2(t)u_2(t). \qquad (A5)$$

Data availability

Software for the proposed method has been developed on a GitHub repository (https://github.com/akuhara/HypoTremorMCMC) and the specific version used for producing the results of this study is archived at the Zenodo repository (https://doi.org/10.5281/zenodo.8333346). The continuous waveform data from DONET stations are publicly open (National Research Institute for Earth Science and Disaster Resilience, 2019). The continuous waveform data from temporary OBSs are available from the corresponding author upon reasonable request. Tectonic tremor locations determined by Ogiso & Tamaribuchi (2022) is available at Slow Earthquake Database (Kano et al., 2018; http://www-solid.eps.s.u-tokyo.ac.jp/~sloweq/).

Acknowledgments

We thank cruise members of R/V Shinsei-Maru, who played an integral role in acquiring the OBS data. We also thank Shukei Ohyanagi and Atikul Haque Farazi for their assistance during the research cruise and the technical staffs at Earthquake Research Institute, The University of Tokyo, for maintaining OBSs. Comments from Madison Bombardier and an anonymous reviewer helped improve the manuscript.

Author contribution

Takeshi Akuhara:

Conceptualization, Formal analysis, Funding acquisition, Investigation, Methodology, Project administration, Resources, Software, Visualization, Writing – original draft

Yusuke Yamashita:

Data curation, Investigation, Resources, Writing – review & editing

Hiroko Sugioka:

Data curation, Investigation, Resources, Writing – review & editing

Masanao Shinohara:

Data curation, Funding acquisition, Resources, Writing – review & editing

References

Akuhara, T., Tsuji, T., & Tonegawa, T. (2020). Overpressured Underthrust Sediment in the Nankai Trough Forearc Inferred From Transdimensional Inversion of High-Frequency Teleseismic Waveforms. *Geophysical Research Letters*, *47*(15). https://doi.org/10.1029/2020GL088280

Araki, E., Saffer, D. M., Kopf, A. J., Wallace, L. M., Kimura, T., Machida, Y., et al. (2017). Recurring and triggered slow-slip events near the trench at the Nankai Trough subduction megathrust. *Science*, *356*(6343), 1157–1160. https://doi.org/10.1126/science.aan3120

Audet, P., & Kim, Y. H. (2016). Teleseismic constraints on the geological environment of deep episodic slow earthquakes in subduction zone forearcs: A review. *Tectonophysics*, *670*, 1–15. https://doi.org/10.1016/j.tecto.2016.01.005

Bombardier, M., Dosso, S. E., Cassidy, J. F., & Kao, H. (2023). Tackling the challenges of tectonic tremor localization using differential traveltimes and Bayesian inversion. *Geophysical Journal International*, *234*(1), 479–493. https://doi.org/10.1093/gji/ggad086

Brown, K. M., Tryon, M. D., DeShon, H. R., Dorman, L. R. M., & Schwartz, S. Y. (2005). Correlated transient fluid pulsing and seismic tremor in the Costa Rica subduction zone. *Earth and Planetary Science Letters*, *238*(1–2), 189–203. https://doi.org/10.1016/j.epsl.2005.06.055

Cruz-Atienza, V. M., Villafuerte, C., & Bhat, H. S. (2018). Rapid tremor migration and pore-pressure waves in subduction zones. *Nature Communications*, *9*(1). https://doi.org/10.1038/s41467-018-05150-3

Geyer, C. J. (1991). Markov Chain Monte Carlo Maximum Likelihood. *Computing Science and Statistics: Proceedings of the 23rd Symposium on the Interface*, (1), 156–163.

Ghosh, A., Vidale, J. E., Sweet, J. R., Creager, K. C., Wech, A. G., Houston, H., & Brodsky, E. E. (2010). Rapid, continuous streaking of tremor in Cascadia. *Geochemistry, Geophysics, Geosystems*, *11*(12), 1–10. https://doi.org/10.1029/2010GC003305

Hashimoto, Y., Sato, S., Kimura, G., Kinoshita, M., Miyakawa, A., Moore, G. F., et al. (2022). Décollement geometry controls on shallow very low frequency earthquakes. *Scientific Reports*, *12*(1), 2677. https://doi.org/10.1038/s41598-022-06645-2

Hastings, W. K. (1970). Monte Carlo Sampling Methods Using Markov Chains and Their Applications. *Biometrika*, *57*(1), 97. https://doi.org/10.2307/2334940

Houston, H., Delbridge, B. G., Wech, A. G., & Creager, K. C. (2011). Rapid tremor reversals in Cascadia generated by a weakened plate interface. *Nature Geoscience*, *4*(6), 404–409. https://doi.org/10.1038/ngeo1157

Husker, A. L., Kostoglodov, V., Cruz-Atienza, V. M., Legrand, D., Shapiro, N. M., Payero, J. S., et al. (2012). Temporal variations of non-volcanic tremor (NVT) locations in the Mexican subduction zone: Finding the NVT sweet spot. *Geochemistry, Geophysics, Geosystems*, *13*(3). https://doi.org/10.1029/2011GC003916

Ide, S. (2010). Striations, duration, migration and tidal response in deep tremor. *Nature*, *466*(7304), 356–359. https://doi.org/10.1038/nature09251

Ide, S., Beroza, G. C., Shelly, D. R., & Uchide, T. (2007). A scaling law for slow earthquakes. *Nature*, *447*(7140), 76–79. https://doi.org/10.1038/nature05780

Kaneda, Y., Kawaguchi, K., Araki, E., Matsumoto, H., Nakamura, T., Kamiya, S., et al. (2015). Development and application of an advanced ocean floor network system for megathrust earthquakes and tsunamis. In *SEAFLOOR OBSERVATORIES* (pp. 643–662). Berlin, Heidelberg: Springer Berlin Heidelberg. https://doi.org/10.1007/978-3-642-11374-1_25

Kano, M., Aso, N., Matsuzawa, T., Ide, S., Annoura, S., Arai, R., et al. (2018).

Development of a slow earthquake database. *Seismological Research Letters*, *89*(4), 1566–1575. https://doi.org/10.1785/0220180021

Kawaguchi, K., Kaneko, S., Nishida, T., & Komine, T. (2015). Construction of the DONET real-time seafloor observatory for earthquakes and tsunami monitoring. In *SEAFLOOR OBSERVATORIES* (pp. 211–228). Berlin, Heidelberg: Springer Berlin Heidelberg. https://doi.org/10.1007/978-3-642-11374-1_10

Li, K. L., Bean, C. J., Bell, A. F., Ruiz, M., Hernandez, S., & Grannell, J. (2022). Seismic tremor reveals slow fracture propagation prior to the 2018 eruption at Sierra Negra volcano, Galápagos. *Earth and Planetary Science Letters*, *586*, 117533. https://doi.org/10.1016/j.epsl.2022.117533

Lomax, A., & Savvaidis, A. (2022). High-Precision Earthquake Location Using Source-Specific Station Terms and Inter-Event Waveform Similarity. *Journal of Geophysical Research: Solid Earth*, *127*(1). https://doi.org/10.1029/2021JB023190

Maeda, T., & Obara, K. (2009). Spatiotemporal distribution of seismic energy radiation from low-frequency tremor in western Shikoku, Japan. *Journal of Geophysical Research: Solid Earth*, *114*(10), 1–17. https://doi.org/10.1029/2008JB006043

McCausland, W. A., Creager, K. C., La Rocca, M., & Malone, S. D. (2010). Short-term and long-term tremor migration patterns of the Cascadia 2004 tremor and slow slip episode using small aperture seismic arrays. *Journal of Geophysical Research: Solid Earth*, *115*(8). https://doi.org/10.1029/2008JB006063

Metropolis, N., Rosenbluth, A. W., Rosenbluth, M. N., Teller, A. H., & Teller, E. (1953). Equation of State Calculations by Fast Computing Machines. *The Journal of Chemical Physics*, *21*(6), 1087–1092. https://doi.org/10.1063/1.1699114

Mizuno, N., & Ide, S. (2019). Development of a modified envelope correlation method based on maximum - likelihood method and application to detecting and locating deep tectonic tremors in western Japan. *Earth, Planets and Space*. https://doi.org/10.1186/s40623-019-1022-x

Nakano, M., Yabe, S., Sugioka, H., Shinohara, M., & Ide, S. (2019). Event Size Distribution of Shallow Tectonic Tremor in the Nankai Trough. *Geophysical Research Letters*, *46*(11), 5828–5836. https://doi.org/10.1029/2019GL083029

National Research Institute for Earth Science and Disaster Resilience (2019). NIED DONET, National Research Institute for Earth Science and Disaster Resilience, https://doi.org/10.17598/nied.0008

Nishikawa, T., Matsuzawa, T., Ohta, K., Uchida, N., Nishimura, T., & Ide, S. (2019). The slow earthquake spectrum in the Japan Trench illuminated by the S-net seafloor observatories. *Science*, *365*(6455), 808–813.

https://doi.org/10.1126/science.aax5618

Obara, K. (2002). Nonvolcanic Deep Tremor Associated with Subduction in Southwest Japan. *Science*, *296*(5573), 1679–1681. https://doi.org/10.1126/science.1070378

Obara, K., & Kato, A. (2016). Connecting slowearthquakes to huge earthquakes. *Science*, *353*(6296), 253–257. https://doi.org/10.1126/science.aaf1512

Ogiso, M., & Tamaribuchi, K. (2022). Spatiotemporal evolution of tremor activity near the Nankai Trough trench axis inferred from the spatial distribution of seismic amplitudes. *Earth, Planets and Space*. https://doi.org/10.1186/s40623-022-01601-w

Payero, J. S., Kostoglodov, V., Shapiro, N., Mikumo, T., Iglesias, A., Pérez-Campos, X., & Clayton, R. W. (2008). Nonvolcanic tremor observed in the Mexican subduction zone. *Geophysical Research Letters*, *35*(7), 1–6. https://doi.org/10.1029/2007GL032877

Plata-Martinez, R., Ide, S., Shinohara, M., Garcia, E. S., Mizuno, N., Dominguez, L. A., et al. (2021). Shallow slow earthquakes to decipher future catastrophic earthquakes in the Guerrero seismic gap. *Nature Communications*, *12*(1). https://doi.org/10.1038/s41467-021-24210-9

Richards-Dinger, K. B., & Shearer, P. M. (2000). Earthquake locations in southern California obtained using source-specific station terms. *Journal of Geophysical Research*, *105*(B5), 10939. https://doi.org/10.1029/2000JB900014

Rogers, G. (2003). Episodic Tremor and Slip on the Cascadia Subduction Zone: The Chatter of Silent Slip. *Science*, *300*(5627), 1942–1943. https://doi.org/10.1126/science.1084783

Rubin, A. M. (2011). Designer friction laws for bimodal slow slip propagation speeds. *Geochemistry, Geophysics, Geosystems*, *12*(4), 1–22. https://doi.org/10.1029/2010GC003386

Saffer, D. M., & Wallace, L. M. (2015). The frictional, hydrologic, metamorphic and thermal habitat of shallow slow earthquakes. *Nature Geoscience*, *8*(8), 594–600. https://doi.org/10.1038/ngeo2490

Sambridge, M. (2014). A Parallel Tempering algorithm for probabilistic sampling and multimodal optimization. *Geophysical Journal International*, *196*(1), 357–374. https://doi.org/10.1093/gji/ggt342

Takemura, S., Furumura, T., & Saito, T. (2009). Distortion of the apparent S-wave radiation pattern in the high-frequency wavefield: Tottori-Ken Seibu, Japan, earthquake of 2000. *Geophysical Journal International*, *178*(2), 950–961. https://doi.org/10.1111/j.1365-246X.2009.04210.x

Takemura, S., Yabe, S., & Emoto, K. (2020). Modelling high-frequency seismograms at ocean bottom seismometers: Effects of heterogeneous structures on source parameter estimation for small offshore earthquakes and shallow low-frequency tremors. *Geophysical Journal International*, *223*(3), 1708–1723. https://doi.org/10.1093/gji/ggaa404

Takemura, S., Obara, K., Shiomi, K., & Baba, S. (2022). Spatiotemporal Variations of Shallow Very Low Frequency Earthquake Activity Southeast Off the Kii Peninsula, Along the Nankai Trough, Japan. *Journal of Geophysical Research: Solid Earth*, *127*(3). https://doi.org/10.1029/2021JB023073

Todd, E. K., Schwartz, S. Y., Mochizuki, K., Wallace, L. M., Sheehan, A. F., Webb, S. C., et al. (2018). Earthquakes and Tremor Linked to Seamount Subduction During Shallow Slow Slip at the Hikurangi Margin, New Zealand. *Journal of Geophysical Research: Solid Earth*, *123*(8), 6769–6783. https://doi.org/10.1029/2018JB016136

Tsuji, T., Dvorkin, J., Mavko, G., Nakata, N., Matsuoka, T., Nakanishi, A., et al. (2011). V P / V S ratio and shear-wave splitting in the Nankai Trough seismogenic zone: Insights into effective stress, pore pressure, and sediment consolidation. *Geophysics*, *76*(3), WA71–WA82. https://doi.org/10.1190/1.3560018

Tsuji, T., Kamei, R., & Pratt, R. G. (2014). Pore pressure distribution of a mega-splay fault system in the Nankai trough subduction zone: Insight into up-dip extent of the seismogenic zone. *Earth and Planetary Science Letters*, *396*, 165–178. https://doi.org/10.1016/j.epsl.2014.04.011

VanDecar, J. C., & Crosson, R. S. (1990). Determination of teleseismic relative phase arrival times using multi-channel cross-correlation and least squares. *Bulletin of the Seismological Society of America*, *80*(1), 150–169. Retrieved from http://www.bssaonline.org/content/80/1/150.short

Yabe, S., Baba, S., Tonegawa, T., Nakano, M., & Takemura, S. (2021). Seismic energy radiation and along-strike heterogeneities of shallow tectonic tremors at the Nankai Trough and Japan Trench. *Tectonophysics*, *800*, 228714. https://doi.org/10.1016/j.tecto.2020.228714

Yamashita, Y., Yakiwara, H., Asano, Y., Shimizu, H., Uchida, K., Hirano, S., et al. (2015). Migrating tremor off southern Kyushu as evidence for slow slip of a shallow subduction interface. *Science*, *348*(6235), 676–679. https://doi.org/10.1126/science.aaa4242

Supplementary Material

Locating tectonic tremors with uncertainty estimates: Time- and amplitude-difference optimization, wave propagation-based quality control, and Bayesian inversion

Takeshi Akuhara[1], Yusuke Yamashita[2], Hiroko Sugioka[3], Masanao Shinohara[1]

[1]Earthquake Research Institute, The University of Tokyo
[2]Disaster Prevision Research Institute, Kyoto University
[3]Department of Planetology, Graduate School of Science, Kobe University

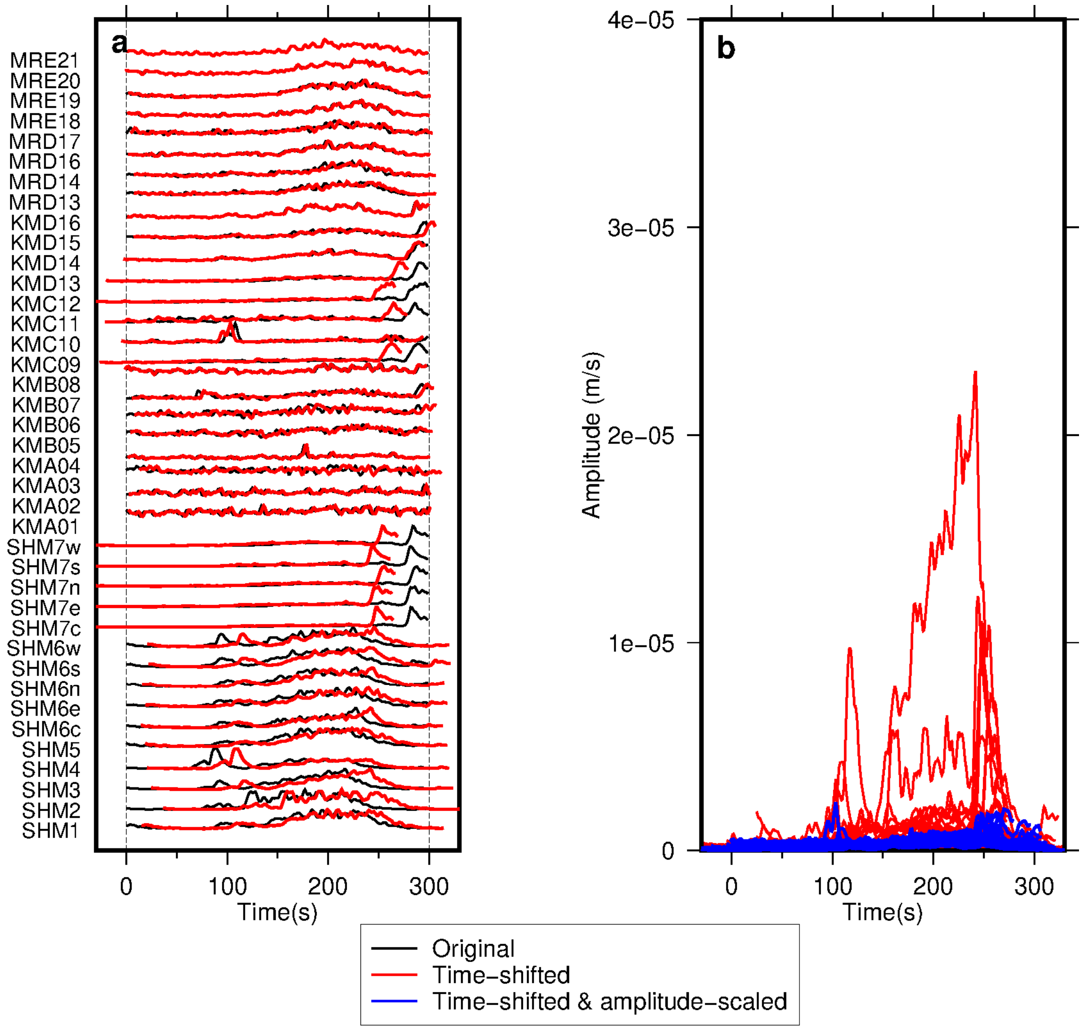

Figure S1. A failure case of the optimization step. Notations are the same as Fig. 3.

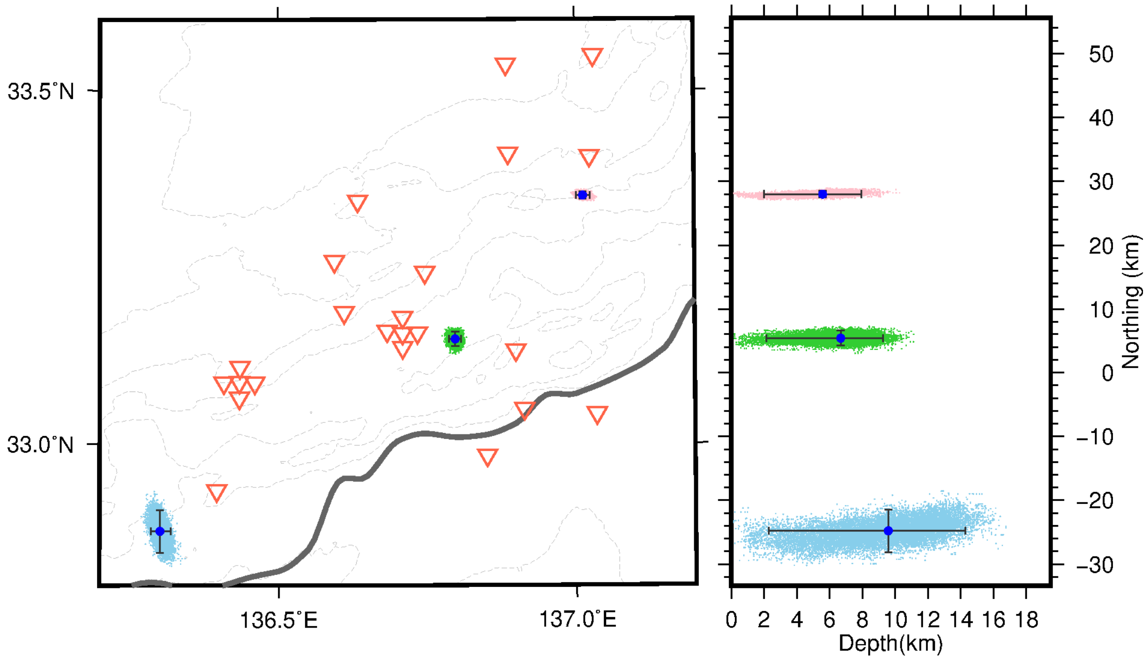

Figure S2. Distribution of MCMC samples for three example events. (Left) Enlarged map view. Pale-blue, green, and pink dots are MCMC samples for each event. The circles and error bars represent the median hypocenters and the 95% confidence interval, respectively. The inverted triangles are stations. The gray line represents the trench. (Right) Cross section view.

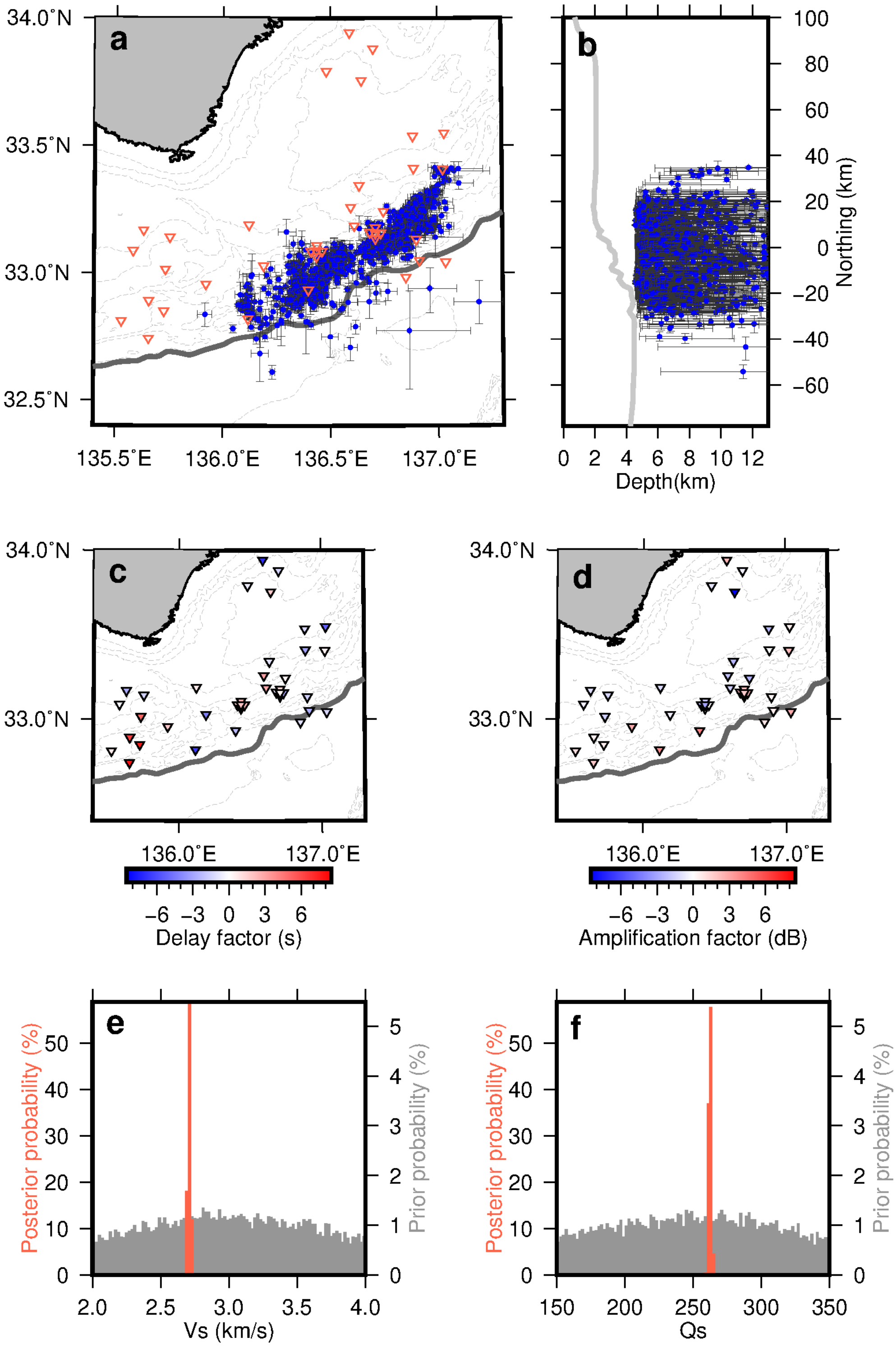

Figure S3. Inversion results where z_0 is set to 4.5 km for the depth prior (see Eq. 19). Notations are the same as Fig. 7.

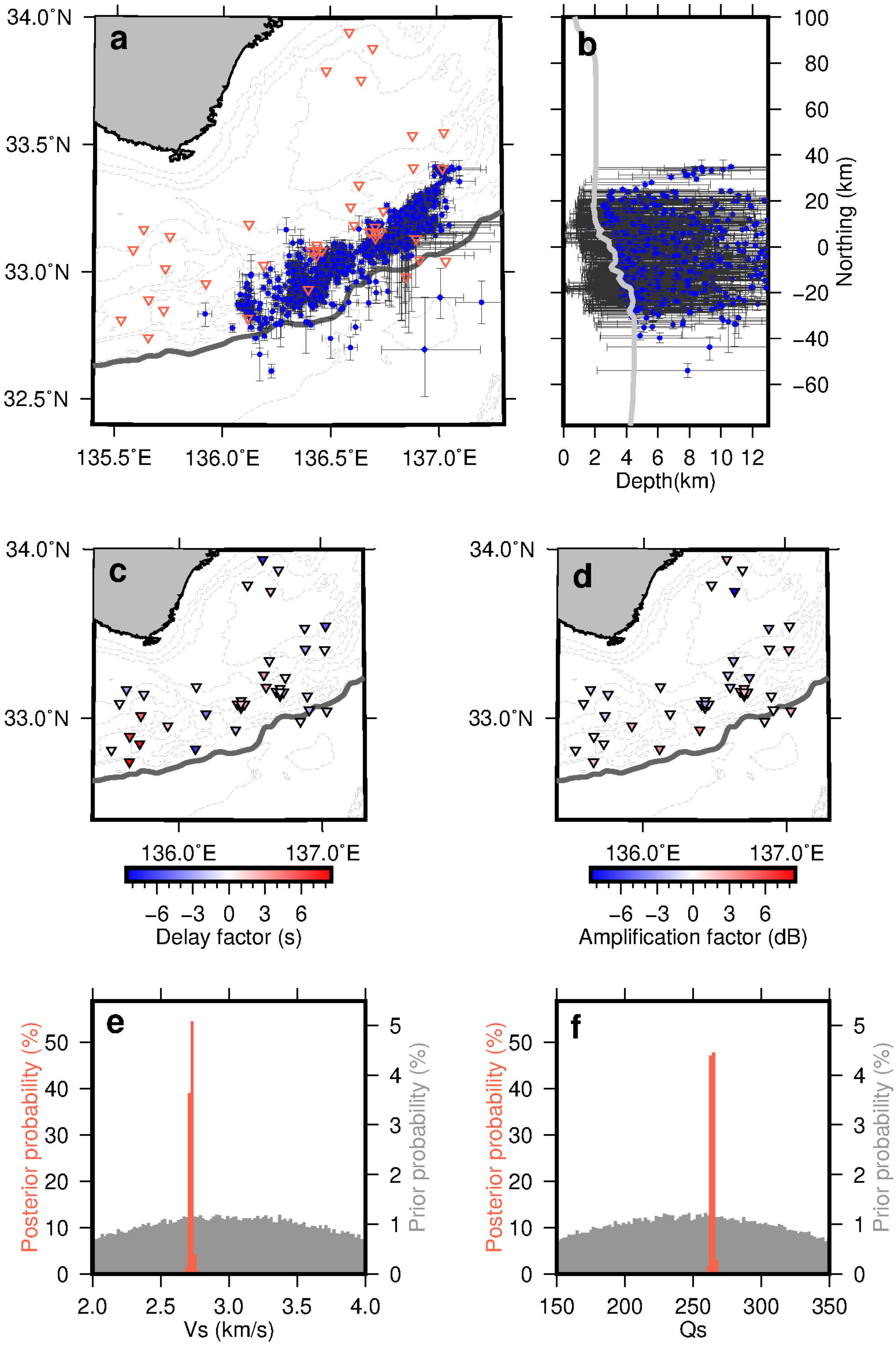

Figure S4. Inversion results without tempering. Notations are the same as Fig. 7.

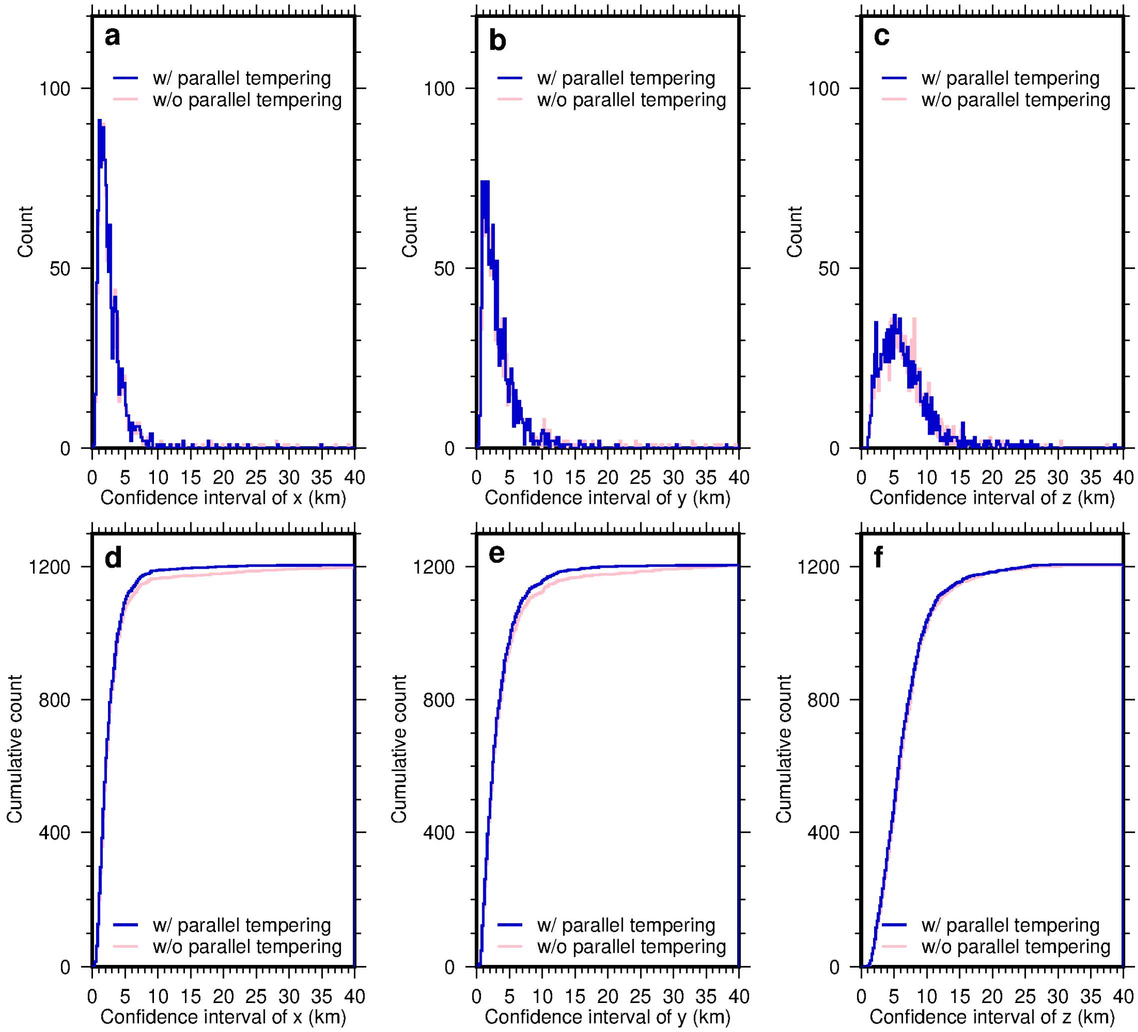

Figure S5. Histograms of the hypocenter uncertainties (i.e., the range of 95% confidence interval) in the (a) east–west, (b) north–south, and (c) vertical directions. The blue and pink lines represent results from tempered and non-tempered analysis, respectively. (d–f) The same as (a–c), but cumulative histograms are shown to highlight the difference between the two analyses.

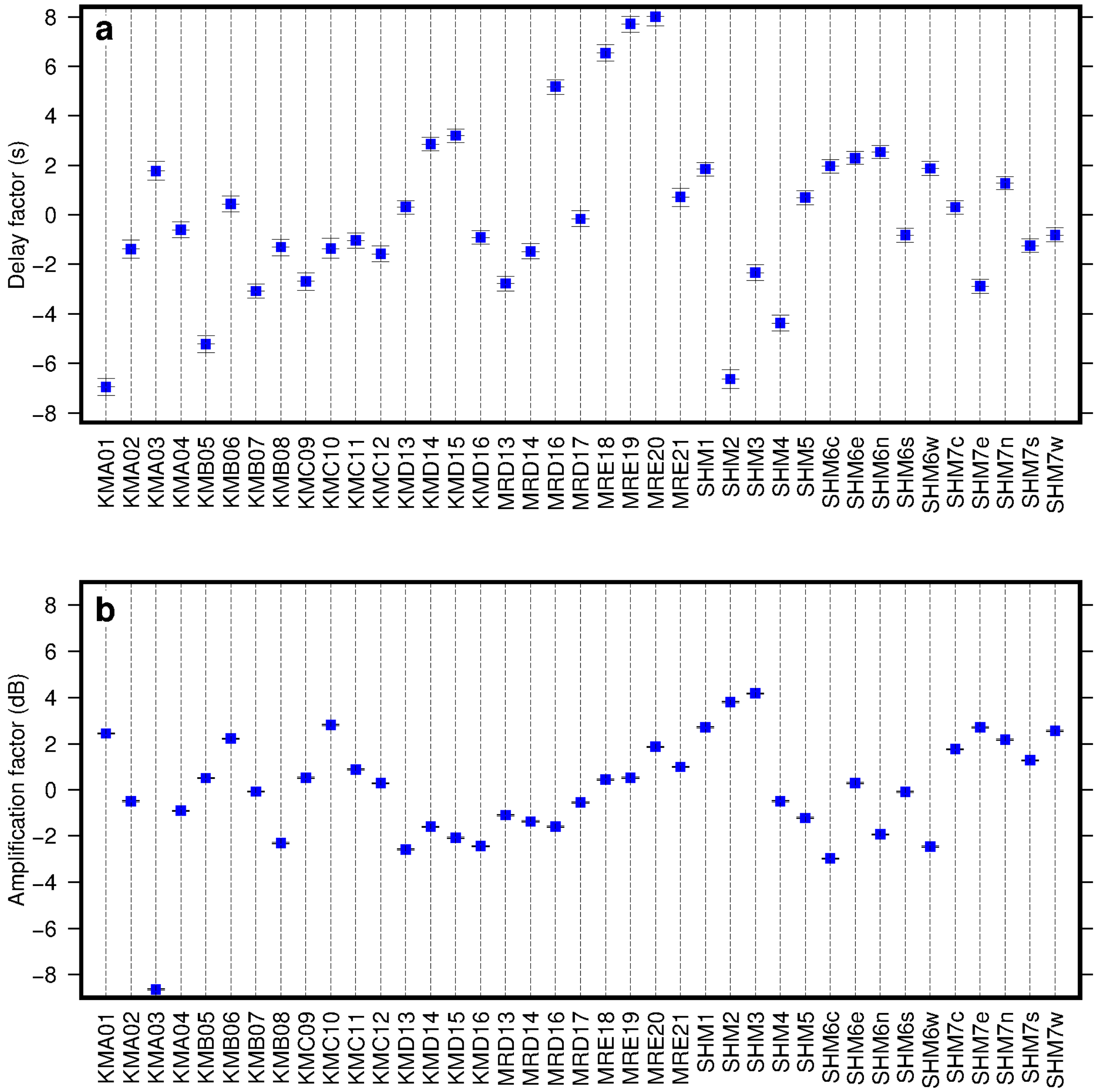

Figure S6. Delay (a) and amplification (b) factors obtained by the inversion analysis. The blue dots show the median value estimated from MCMC samples, with the error bars representing the 95% confidence interval.

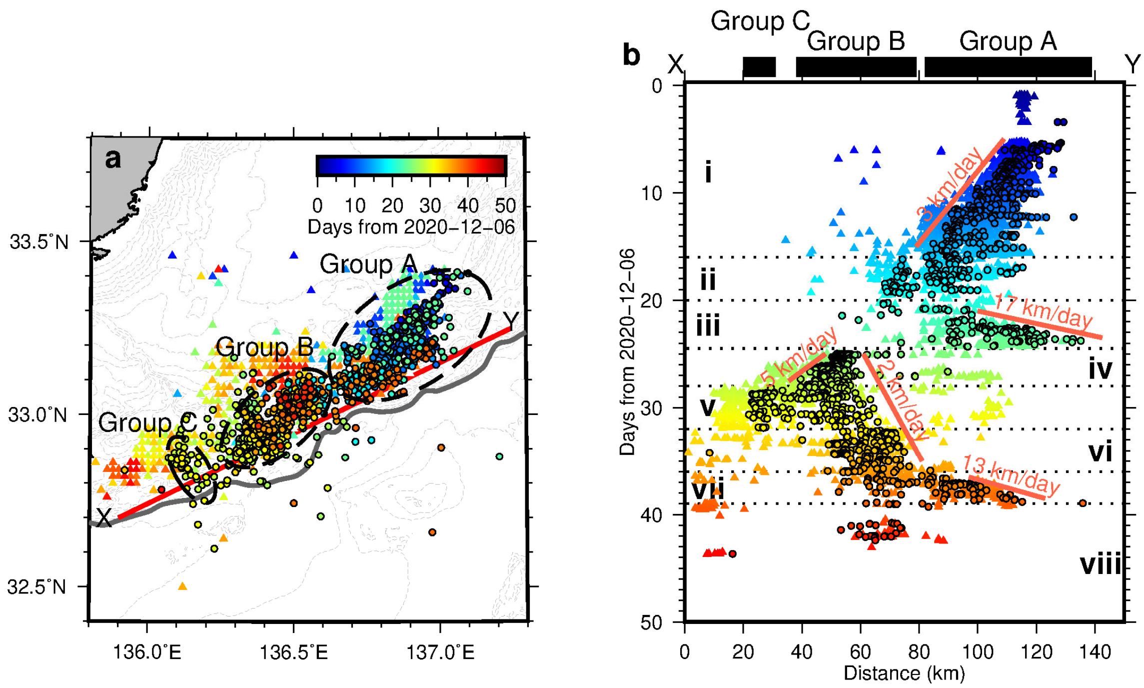

Figure S7. The same as Figure 10 but with the comparison to the results from Ogiso & Tamaribuchi (2022). In both panels (a) and (b), underlying triangles represent tremor epicenters determined by Ogiso & Tamaribuchi (2022).